between the binding change and second injection was within 5 min, the effect of the timing of the BP_{ND} reduction was slight.

Interval between the dual injections

In the simulation study with noise for the ROI-based estimation, a dual-injection scan with a 30 min injection interval, gave unbiased and reliable BP_{ND1} and BP_{ND2} estimates (Fig. 5). In the 70% reduction TAC, the COV of ΔBP_{ND} was less than 5% when the injection interval was 30 min. Conversely, results from the 30% reduction TAC showed that a 50 min interval would be required to estimate ΔBP_{ND} within a 5% COV. In this study, we evaluated the reliability of BP_{ND} estimates for an ROI-based estimation. However, in voxel-based estimations, the noise level is usually higher, so the COV of estimates can be expected to increase.

In the ROI analysis of human study with single injection, it is reported that a 30 min scan of [^{11}C]raclopride gave unbiased and reliable BP_{ND} estimates (Ikoma et al., 2008). The kinetics of [^{11}C]raclopride in the human brain is different from that in the monkey brain, inducing the difference in required scan durations. The required injection interval for a reliable estimation depends on the kinetics of the ligand, the magnitude of ΔBP_{ND} and the noise level according to injection dose, ROI size, sensitivity of the measurement system, and so on. Therefore, evaluating the effect of the injection interval on the reliability of parameter estimates is important.

Monkey studies

In the simulation studies, it was demonstrated that the MI-SRTM approach could detect a change in BP_{ND} caused by the release of a dopamine pulse or by the increase in administered raclopride. Furthermore, we demonstrated the validity of the proposed method using actual data from monkeys. As a result, the estimated BP_{ND} reduction changed according to the injected mass of raclopride in the second injection, and this is consistent with the results from the simulation studies. We are planning further studies on monkeys with co-injection of various amount of cold raclopride to examine the relationship between the observed changes in BP_{ND} and the occupancy of receptors. Furthermore, using the present approach, it may be possible to estimate endogenous dopamine release by pharmaceutical stimuli although the interpretation of the results must be made with caution because the level of endogenous dopamine is sensitive to the timing and the response of pharmaceutical manipulation (Yoder et al., 2004).

Potential of the multiple-injection approach

The dual-injection approach is able to assess the change in BP_{ND} for receptor competition studies in a single PET scan and shortened study period, as compared to a conventional approach. However, this approach requires some caution. Firstly, the error due to residual radioactivity at the time of the second injection may affect the reliability of BP_{ND2} estimates. Therefore, we estimated the residual radioactivity, not from the measured TAC, but from a fitted TAC from the first injection. In the simulation study, with noise-added TACs, the bias and COV of BP_{ND2} estimated from the second injection were acceptable (Fig. 5).

Secondly, the administered molar amount of second injection must be same as that of the first injection for the evaluation of dopamine release, because the value of BP_{ND} decreases according to the increase in administered raclopride even if the dopamine pulse does not be released (Fig. 2B). In addition, in the dual-injection study, the radioligand for the first injection remains in the tissue at the time of second injection. Therefore, the molar amount of administered raclopride needs to be sufficiently small, that is to say, the specific activity of administered [^{11}C]raclopride should be high enough. The mass of first injection is required to be less than about 1 nmol/kg so that the remained raclopride at the second injection does not affect BP_{ND2} estimates (data not shown). To keep the amount of administered raclopride below 1 nmol/kg with the administration of 37MBq/kg [^{11}C]raclopride, its specific activity should be greater than 37 GBq/μmol. However, in the multiple-injection study, if one can synthesize [^{11}C]raclopride with high specific activity, it is an advantage that [^{11}C]raclopride, synthesized once before the scan, can be administered for both the first and second injections.

Thirdly, the timing of the second injection affected the BP_{ND} estimates, as it was also observed in the estimations using two separate conventional scans. The timing of the second injection should be fixed within the intersubjects of the group, and the interpretation of the ΔBP_{ND} requires some caution when a time–activity curve of free [^{11}C]raclopride differs. The competition paradigm also should be applied carefully in case where the dopamine released slowly in response to stimuli, because it is often difficult to estimate the timing of the dopamine peak. Despite this, we have shown that the multiple-injection approach can be used to determine a reduction in BP_{ND} values as effectively as using two separate scans, but within a single scan lasting 100 min.

The ESRTM approach can also provide ΔBP_{ND} values from a single-session scan by administering [^{11}C]raclopride using a bolus-plus-continuous (B/I) infusion approach (Zhou et al., 2006). Meanwhile, with the MI-SRTM approach, [^{11}C]raclopride can be administered several times by bolus injection, so there is no need to control the administered dose continuously, and it is easy to change the administered mass of raclopride significantly during the scan.

Since the MI-SRTM is a successor of SRTM, one advantage of the MI-SRTM is that the BP_{ND} parametric map can be obtained as shown in Fig. 8, which is crucial to perform statistical parametric mapping (SPM) type analysis. The results of our simulation and monkey studies suggest that the MI-SRTM can be applied to the estimation of ΔBP_{ND} for human study, though the optimal injection protocol needs to be evaluated. One application of the MI-SRTM approach for the human study is to estimate occupancy within short period. By the MI-SRTM approach, one can estimate the BP_{ND} value without antipsychotics and BP_{ND} with antipsychotics from one session of PET study. This approach is also useful in the estimation of receptor density (B_{max}) and affinity (K_d) that normally requires several scans with variable masses of raclopride injections (Farde et al., 1986; Doudet et al., 2003). Furthermore, this approach can be applied to other PET ligands if the BP_{ND} can be estimated by the SRTM approach.

In summary, we have developed a method for estimating the change in binding potential in a single PET scan using multiple injections of [^{11}C]raclopride and a simplified reference tissue model. Our simulations showed that the reduction in BP_{ND}, estimated by this approach, was related to the amount of released dopamine or to the administered mass of raclopride. We also demonstrated that the reduction in BP_{ND} varied according to the increase in administered raclopride in monkey studies. The proposed method, with multiple injections, has potential for use in quantitatively assessing the change in specific binding, in a short study period, for several neurotransmitter competition studies.

Acknowledgments

This research was supported by the Ministry of Education, Culture, Sports, Science and Technology, Grant-in-Aid for Young Scientists (B) (No.20790839), Japan, Kobe Cluster I and II, Ministry of Education, Culture, Sports, Science and Technology of Japan (MEXT; T.H.), and the MHLW (Ministry of Health, Labour and Welfare of Japan) Health Science Research Grant, H17-025 (T.H., H,I).

We are grateful to members of the Department of Investigative Radiology, National Cardiovascular Center Research Institute, for their support of the PET experiment and for helpful suggestions.

Please cite this article as: Ikoma, Y., et al., Quantitative evaluation of changes in binding potential with a simplified reference tissue model and multiple injections of [^{11}C]raclopride, NeuroImage (2009), doi:10.1016/j.neuroimage.2009.05.099

Appendix A

The multiple-injection simplified reference tissue model is based on the following differential equations of the simplified reference tissue model on the assumption that the time–activity curves of the target and reference tissues can be fitted to a single tissue compartment model with plasma input (Lammertsma and Hume, 1996)

$$\frac{dC_t}{dt} = K_1 C_p(t) - k_{2a} C_t(t) \tag{A1}$$

$$\frac{dC_r}{dt} = K_1^r C_p(t) - k_2^r C_t(t) \tag{A2}$$

$$K_1 / k_{2a} = K_1 / k_2 \cdot (1 + \mathrm{BP_{ND}}) \tag{A3}$$

where C_p is the metabolite corrected plasma concentration, C_t and C_r are the concentration in target and reference tissue, respectively, k_{2a} (min^{-1}) is the apparent (overall) rate constant for transfer from specific compartment to plasma in the target tissue.

Eqs. (A1) and (A2) are expressed as follows by Laplace transform:

$$sC_t(s) - C_t(0) = K_1 C_p(s) - k_{2a} C_t(s) \tag{A4}$$

$$sC_r(s) - C_r(0) = K_1^r C_p(s) - k_2^r C_t(s) \tag{A5}$$

where $C_t(0)$ and $C_r(0)$ are the total concentration in target and reference tissue, respectively, at the time of injection.

From Eqs. (A4),(A5) and the assumption $K_1^r / k_2^r = K_1 / k_2$, the following expression can be derived:

$$C_t(s) = R_1 C_r(s) + \frac{1}{s + k_{2a}}(k_2 - R k_{2a}) C_r(s) + \frac{1}{s + k_{2a}}(C_t(0) - R_1 C_r(0)). \tag{A6}$$

From Eqs. (A3) and (A6), the following expression can be derived by inverse-Laplace transform:

$$C_t(t) = R_1 C_r(t) + \left(k_2 - \frac{R_1 k_2}{1 + \mathrm{BP_{ND}}}\right) e^{-\frac{k_2}{1 + \mathrm{BP_{ND}}} t} \otimes C_r(t) + (C_t(0) - R_1 C_r(0)) e^{-\frac{k_2}{1 + \mathrm{BP_{ND}}} t}. \tag{A7}$$

In the second injection, R_1, k_2, and $\mathrm{BP_{ND}}$ can be estimated by giving $C_t(t)$, $C_r(t)$, and $C_t(0)$ and $C_r(0)$ at the time of second injection. Meanwhile, in the first injection, $C_t(0)$ and $C_r(0)$ are 0 at the time of first injection, so $C_t(t)$ can be expressed as follows:

$$C_t(t) = R_1 C_r(t) + \left(k_2 - \frac{R_1 k_2}{1 + \mathrm{BP_{ND}}}\right) e^{-\frac{k_2}{1 + \mathrm{BP_{ND}}} t} \otimes C_r(t). \tag{A8}$$

References

Breier, A., Su, T.P., Saunders, R., Carson, R.E., Kolachana, B.S., de Bartolomeis, A., Weinberger, D.R., Weisenfeld, N., Malhotra, A.K., Eckelman, W.C., Pickar, D., 1997. Schizophrenia is associated with elevated amphetamine-induced synaptic dopamine concentrations: evidence from a novel positron emission tomography method. Proc. Natl. Acad. Sci. U.S.A. 94, 2569–2574.

Carson, R.E., Breier, A., de Bartolomeis, A., Saunders, R.C., Su, T.P., Schmall, B., Der, M.G., Pickar, D., Eckelman, W.C., 1997. Quantification of amphetamine-induced changes in [^{11}C]raclopride binding with continuous infusion. J. Cereb. Blood Flow Metab. 17, 437–447.

Christian, B.T., Narayanan, T., Shi, B., Morris, E.D., Mantil, J., Mukherjee, J., 2004. Measuring the in vivo binding parameters of [18F]-fallypride in monkeys using a PET multiple-injection protocol. J. Cereb. Blood Flow Metab. 24, 309–322.

Delforge, J., Pappata, S., Millet, P., Samson, Y., Bendriem, B., Jobert, A., Crouzel, C., Syrota, A., 1995. Quantification of benzodiazepine receptors in human brain using PET, [^{11}C] flumazenil, and a single-experiment protocol. J. Cereb. Blood Flow Metab. 15, 284–300.

Doudet, D.J., Jivan, S., Holden, J.E., 2003. In vivo measurement of receptor density and affinity: comparison of the routine sequential method with a nonsequential method in studies of dopamine D_2 receptors with [^{11}C]raclopride. J. Cereb. Blood Flow Metab. 23, 280–284.

Endres, C.J., Kolachana, B.S., Saunders, R.C., Su, T., Weinberger, D., Breier, A., Eckelman, W.C., Carson, R.E., 1997. Kinetic modeling of [^{11}C]raclopride: combined PET-microdialysis studies. J. Cereb. Blood Flow Metab. 17, 932–942.

Endres, C.J., Carson, R.E., 1998. Assessment of dynamic neurotransmitter changes with bolus or infusion delivery of neuroreceptor ligands. J. Cereb. Blood Flow Metab. 18, 1196–1210.

Farde, L., Ehrin, E., Eriksson, L., Greitz, T., Hall, H., Hedstrom, C.G., Litton, J.E., Sedvall, G., et al., 1985. Substituted benzamides as ligands for visualization of dopamine receptor binding in the human brain by positron emission tomography. Proc. Natl. Acad. Sci. U.S.A. 82, 3863–3867.

Farde, L., Hall, H., Ehrin, E., Sedvall, G., 1986. Quantitative analysis of D_2 dopamine receptor binding in the living human brain by PET. Science 231, 258–261.

Gallezot, J.D., Bottlaender, M.A., Delforge, J., Valette, H., Saba, W., Dollé, F., Coulon, C.M., Ottaviani, M.P., Hinnen, F., Syrota, A., Grégoire, M.C., 2008. Quantification of cerebral nicotinic acetylcholine receptors by PET using 2-[^{18}F]fluoro-A-85380 and the multiinjection approach. J. Cereb. Blood Flow Metab. 28, 172–189.

Gunn, R.N., Lammertsma, A.A., Hume, S.P., Cunningham, V.J., 1997. Parametric imaging of ligand–receptor binding in PET using a simplified reference region model. Neuroimage 6, 279–287.

Hall, H., Köhler, C., Gawell, L., Farde, L., Sedvall, G., 1988. Raclopride, a new selective ligand for the dopamine-D2 receptors. Prog. Neuropsychopharmacol. Biol. Psychiatry 12, 559–568.

Herzog, H., Tellmann, L., Hocke, C., Pietrzyk, U., Casey, M.E., Kuwert, T., 2004. NEMA NU2-2001 guided performance evaluation of four Siemens ECAT PET scanners. IEEE Trans. on. Nucl. Science 51, 2662–2669.

Ikoma, Y., Toyama, H., Suhara, T., 2004. Simultaneous quantification of two brain functions with dual tracer injection in PET dynamic study. In: Iida, H., Shah, N.J., Hayashi, T., Watabe, H. (Eds.), Quantitation in Biomedical Imaging with PET and MRI. InElsevier, pp. 74–78.

Ikoma, Y., Ito, H., Arakawa, R., Okumura, M., Seki, C., Shidahara, M., Takahashi, H., Kimura, Y., Kanno, I., Suhara, T., 2008. Error analysis for PET measurement of dopamine D_2 receptor occupancy by antipsychotics with [^{11}C]raclopride and [^{11}C] FLB457. Neuroimage 42, 1285–1294.

Kim, K.M., Watabe, H., Hayashi, T., Hayashida, K., Katafuchi, T., Enomoto, N., Ogura, T., Shidahara, M., Takikawa, S., Eberl, S., Nakazawa, M., Iida, H., 2006. Quantitative mapping of basal and vasareactive cerebral blood flow using split-dose ^{123}I-iodoamphetamine and single photon emission computed tomography. Neuroimage 33, 1126–1135.

Koepp, M.J., Gunn, R.N., Lawrence, A.D., Cunningham, V.J., Dagher, A., Jones, T., Brooks, D.J., Bench, C.J., Grasby, P.M., 1998. Evidence for striatal dopamine release during a video game. Nature 393, 266–268.

Koeppe, R.A., Raffel, D.M., Snyder, S.E., Ficaro, E.P., Kilbourn, M.R., Kuhl, D.E., 2001. Dual-[11C]tracer single-acquisition positron emission tomography studies. J. Cereb. Blood Flow Metab. 21, 1480–1492.

Köhler, C., Hall, H., Ogren, S.O., Gawell, L., 1985. Specific in vitro and in vivo binding of 3H-raclopride. A potent substituted benzamide drug with high affinity for dopamine D-2 receptors in the rat brain. Biochem. Pharmacol. 34, 2251–2259.

Lammertsma, A.A., Hume, S.P., 1996. Simplified reference tissue model for PET receptor studies. Neuroimage 4, 153–158.

Lammertsma, A.A., Bench, C.J., Hume, S.P., Osman, S., Gunn, K., Brooks, D.J., Frackowiak, R.S., 1996. Comparison of methods for analysis of clinical [^{11}C]raclopride studies. J. Cereb. Blood Flow Metab. 16, 42–52.

Laruelle, M., Iyer, R.N., al-Tikriti, M.S., Zea-Ponce, Y., Malison, R., Zoghbi, S.S., Baldwin, R.M., Kung, H.F., Charney, D.S., Hoffer, P.B., Innis, R.B., Bradberry, C.W., 1997. Microdialysis and SPECT measurements of amphetamine-induced dopamine release in nonhuman primates. Synapse 25, 1–14.

Logan, J., Fowler, J.S., Volkow, N.D., Ding, Y.S., Wang, G.J., Alexoff, D.L., 2001. A strategy for removing the bias in the graphical analysis method. J. Cereb. Blood Flow Metab. 21, 307–320.

Millet, P., Delforge, J., Mauguiere, F., Pappata, S., Cinotti, L., Frouin, V., Samson, Y., Bendriem, B., Syrota, A., 1995. Parameter and index images of benzodiazepine receptor concentration in the brain. J. Nucl. Med. 36, 1462–1471.

Mintun, M.A., Raichle, M.E., Kilbourn, M.R., Wooten, G.F., Welch, M.J., 1984. A quantitative model for the in vivo assessment of drug binding sites with positron emission tomography. Ann. Neurol. 15, 217–227.

Morris, E.D., Babich, J.W., Alpert, N.M., Bonab, A.A., Livni, E., Weise, S., Hsu, H., Christian, B.T., Madras, B.K., Fischman, A.J., 1996a. Quantification of dopamine transporter density in monkeys by dynamic PET imaging of multiple injections of ^{11}C-CFT. Synapse 24, 262–272.

Morris, E.D., Alpert, N.M., Fischman, A.J., 1996b. Comparison of two compartmental models for describing receptor ligand kinetics and receptor availability in multiple injection PET studies. J. Cereb. Blood Flow. Metab. 16, 841–853.

Muzic, R.R., Nelson, A.D., Saidel, G.M., Miraldi, F., 1996. Optimal experiment design for PET quantification of receptor concentration. IEEE Trans. Med. Imaging 15, 2–12.

Yoder, K.K., Wang, C., Morris, E.D., 2004. Change in binding potential as a quantitative index of neurotransmitter release is highly sensitive to relative timing and kinetics of the tracer and the endogenous ligand. J. Nucl. Med. 45, 903–911.

Watabe, H., Endres, C.J., Breier, A., Schmall, B., Eckelman, W.C., Carson, R.E., 2000. Measurement of dopamine release with continuous infusion of [^{11}C]raclopride: optimization and signal-to-noise considerations. J. Nucl. Med. 41, 522–530.

Watabe, H., Ohta, Y., Teramoto, N., Miyake, Y., Kurokawa, M., Yamamoto, A., Ose, Y., Hayashi, T., Iida, H., 2006. A novel reference tissue approach for multiple injections of [C-11]Raclopride. Neuroimage 31 (Suppl. 2), T73.

Zhou, Y., Chen, M.K., Endres, C.J., Ye, W., Brasic, J.R., Alexander, M., Crabb, AH, Guilarte, TR, Wong, D.F., 2006. An extended simplified reference tissue model for the quantification of dynamic PET with amphetamine challenge. Neuroimage 33, 550–563.

Please cite this article as: Ikoma, Y., et al., Quantitative evaluation of changes in binding potential with a simplified reference tissue model and multiple injections of [^{11}C]raclopride, NeuroImage (2009), doi:10.1016/j.neuroimage.2009.05.099

Ann Nucl Med
DOI 10.1007/s12149-009-0272-2

ORIGINAL ARTICLE

Evaluation of utility of asymmetric index for count-based oxygen extraction fraction on dual-tracer autoradiographic method for chronic unilateral brain infarction

Katsuhiro Iwanishi · Hiroshi Watabe · Hiroshi Fujisaki · Takuya Hayashi · Yoshinori Miyake · Kotaro Minato · Masaki Naganuma · Toshiyuki Uehara · Chiaki Yokota · Hiroshi Moriwaki · Katsufumi Kajimoto · Kazuhito Fukushima · Kazuo Minematsu · Hidehiro Iida

Received: 1 April 2009 / Accepted: 28 April 2009

Abstract

Objective For diagnosing patients with ischemic cerebrovascular disease, non-invasive count-based method with $^{15}O_2$ and $H_2^{15}O$ positron-emission tomography (PET) data is widely used to measure asymmetric increases in oxygen extraction fraction (OEF). For shortening study time, we have proposed dual-tracer autoradiographic (DARG) protocol in which $^{15}O_2$ gas and $C^{15}O_2$ gas are sequentially administrated within short period. In this paper, we evaluated feasibility of the non-invasive count-based method with the DARG protocol.

Methods Twenty-three patients [67.8 ± 9.9 (mean ± SD) years] with chronic unilateral brain infarction were examined by the use of measurements of asymmetric OEF elevation. As DARG protocol, $^{15}O_2$ and $C^{15}O_2$ gases were inhaled with 5-min interval and dynamic PET data were acquired for 8 min. Quantitative OEF (qOEF) image was computed with PET data and arterial input function. Ratio image of $^{15}O_2$ and $C^{15}O_2$ phases of PET data was computed as count-based OEF (cbOEF) image. The asymmetric indices (AI) of qOEF (qOEF-AI) and cbOEF (cbOEF-AI) were obtained from regions of interest symmetric placed on left and right sides of cerebral hemisphere. To optimize the summation time of PET data for the cbOEF image, qOEF and cbOEF images with various summation times were compared.

Results Image quality of cbOEF image was better than that of qOEF image. The best correlation coefficient of 0.94 was obtained when the cbOEF image was calculated from 0 to 180 s of $^{15}O_2$ summed image and 340 to 440 s of $C^{15}O_2$ summed image.

Conclusion Using the appropriate summation time, we obtained the cbOEF image with good correlation with qOEF image, which suggests non-invasive cbOEF image can be used for evaluating the degree of misery perfusion in patients with chronic unilateral brain infarction. The count-based method with DARG protocol has a potential to dramatically reduce the examination time of ^{15}O PET study.

Keywords Dual-tracer autoradiographic method · Count-based method · Oxygen extraction fraction · Asymmetric index

K. Iwanishi (✉) · H. Watabe · T. Hayashi · H. Iida
Department of Investigative Radiology,
National Cardiovascular Center Research Institute,
5-7-1 Fujishirodai, Suita, Osaka 565-8565, Japan
e-mail: kiwanish@ri.ncvc.go.jp

K. Iwanishi · K. Minato
Informatics Science, Nara Institute of Science and Technology,
Nara, Japan

H. Fujisaki · Y. Miyake · K. Fukushima
Department of Radiology and Nuclear Medicine,
National Cardiovascular Center Hospital, Osaka, Japan

M. Naganuma · T. Uehara · C. Yokota · H. Moriwaki · K. Kajimoto · K. Minematsu
Department of Cerebrovascular Medicine,
National Cardiovascular Center Hospital, Osaka, Japan

Introduction

Positron-emission tomography (PET) with oxygen 15 compounds can quantitatively generate the brain functional images of cerebral blood flow (CBF), oxygen extraction fraction (OEF), cerebral metabolic rate of oxygen ($CMRO_2$), and cerebral blood volume (CBV). These images are the important indices for diagnosing cerebrovascular diseases [1]. In particular, OEF image is used to

Published online: 16 June 2009

diagnose the diseases and an index of the prediction of stroke risk [2–7].

These functional images are usually computed by either steady-state method (SS method) [8–12] or autoradiographic method (ARG method) [13–18]. In SS method, quantitative images are estimated from data acquired while in the steady state reached during the continuous inhalation of $^{15}O_2$ and $C^{15}O_2$ gases. The study period with this method is long (approximately 2 h) due to the waiting time needed to reach equilibrium. The ARG method uses separate administrations of three traces of CO, CO_2, and O_2 gases [17]. The study period with the ARG method is shorter than that need with the SS method. However, a study with the ARG method still takes more than half an hour, because there is a waiting time for the decay of the residual radioactivity of the preceding tracer used. Lately, Kudomi et al. developed a dual-tracer autoradiographic method (DARG) method to shorten the PET study period [19]. This method used a single PET scan with the sequential administration of dual tracers of $^{15}O_2$ and $C^{15}O_2$ gases ($^{15}O_2$–$C^{15}O_2$ scan), and generated CBF, OEF, and $CMRO_2$ images simultaneously in an autoradiographic manner.

All methods described above require arterial blood sampling for generation of these functional images. The arterial blood sampling is labor intensive and has the possibility of blood infection. Alternatively, the ratio image of $^{15}O_2$ counts and $C^{15}O_2$ (or $H_2^{15}O$) counts assumes to be represented as relative OEF image (count-based OEF, cbOEF) [20], and has been used as the substitution of quantitative OEF (qOEF) image [5, 7, 21–24]. By the cbOEF image, one can non-invasively evaluate asymmetric increase in OEF value with a simple calculation [6, 21, 22, 24]. Recently, Kobayashi et al. investigated the optimal scan protocol for computing cbOEF to diagnose misery perfusion [25]. They concluded the cbOEF could appropriately diagnose misery perfusion when they used $^{15}O_2$ counts from 4 min after $^{15}O_2$ gas inhalation to 7 min and $H_2^{15}O$ counts for 3 min after injection of $H_2^{15}O$. In their study, continuous inhalation of $^{15}O_2$ gas and bolus injection of $H_2^{15}O$ was utilized for the administration of tracers.

In this study, we investigated the feasibility of cbOEF obtained by the DARG protocol that consists of sequential administrations of $^{15}O_2$ and $C^{15}O_2$ gases. We computed both cbOEF and qOEF images from actual PET data and both images were compared. Although, in general, the ratio image of $^{15}O_2$ counts and $C^{15}O_2$ counts is known to be proportional to qOEF image, the ratio image on the DARG protocol is special due to contamination of residual radioactivity of $^{15}O_2$ gas after inhalation of $C^{15}O_2$ gas. Therefore, we investigated the optimized range of summation time for $^{15}O_2$ counts and $C^{15}O_2$ counts in order to obtain the ratio image proportional to qOEF image. Using the DARG protocol, further shortening of examination time expects to be archived.

Materials and methods

Subjects

Subjects were 23 patients [15 men and 8 women; age (mean ± SD) 67.8 ± 9.9 years] with chronic unilateral brain infarction, which increased OEF on the unilateral side of the brain, and decreased CBF on the ipsilateral side of the brain. Selection of the data was made by visual inspection. Written informed consent was obtained from each subject prior to the study.

PET procedure

Figure 1 shows a schematic diagram of the clinical study protocol with the DARG method for our institute. The PET scanner we used was ECAT EXACT47 (CTI Inc., Knoxville, TN, USA). First, a 10-min transmission scan was performed to correct gamma ray attenuation. Then, $C^{15}O$ gas of 2500 MBq was inhaled for 30 s, and 90 s post-inhalation, a 4-min emission scan ($C^{15}O$ scan) was performed to obtain a CBV image as well as to correct vascular space in the DARG method. Finally, a single dynamic PET scan was performed with the sequential inhalation of $^{15}O_2$ gas (4000 MBq) and $C^{15}O_2$ gas (5,000 MBq) in 5-min time interval. Their inhalation period was 1 min. All radioactive gases were provided through a face mask.

For qOEF calculation, it is necessary to measure the arterial radioactivity curve as an arterial input function (AIF). A catheter was inserted into the brachial artery of the patient. As AIF, the radioactivity in the arterial blood during a $^{15}O_2$–$C^{15}O_2$ scan was continuously monitored by a GSO detector [26], with a flow rate of 3.5 ml/min. The inner diameter of the tube was approximately 2 mm, and the distance from the catheter to the detector was 20–25 cm. The arterial blood was sampled at the beginning

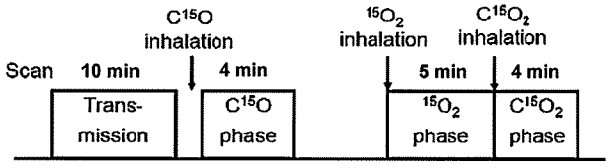

Fig. 1 The schematic diagram of clinical protocol and time schedule of DARG-PET study. The PET scan times for $C^{15}O$ and $^{15}O_2$–$C^{15}O_2$ were 4 and 8 min. The start time of $C^{15}O$ PET scan was the inhalation start time after 30 s, and the $^{15}O_2$–$C^{15}O_2$ scan start time was same the start time of inhaling $^{15}O_2$ gas

of the $C^{15}O$ scan for 30 s and the radioactivity concentration in the arterial blood was measured by a Well counter system (Shimadzu Corporation, Kyoto, Japan). The radioactivity in the sample measured by the Well counter was utilized for computing CBV image and cross-calibration between the Well counter and the GSO detector.

Quantitative OEF image

Quantitative OEF image was calculated using PET counts during $^{15}O_2$ phase $\left(\int_O C_i(t)dt\right)$ and during $C^{15}O_2$ phase $\left(\int_W C_i(t)dt\right)$, and AIF by the DARG method. The detail of the DARG method is found elsewhere [19, 27]. In brief, at first, the AIF was separated into $^{15}O_2$ ($A_{O_2}(t)$) component and $H_2^{15}O$ ($A_{H_2O}(t)$) component (note that although we used $C^{15}O_2$ gas, we used $H_2^{15}O$ for the expression in this section due to the rapid exchange of $H_2^{15}O$ by carbonate dehydratase in the lung). Then, CBF (f) was estimated using a look-up table procedure using the following equation:

$$\begin{aligned}\int_W Ci(t)dt =& f\int_W A_{H_2O}(t)\otimes \exp^{-\frac{f}{p}t}dt + V_B \\ &\cdot R_{Hct}\int_W A_{O_2}(t)dt \\ &+\left(f\int_W A_{O_2}(t)\otimes \exp^{-\frac{f}{p}t}dt + V_B\cdot R_{Hct}\cdot F_v\int_W A_{O_2}(t)dt\right) \\ &\times \frac{\int_O Ci(t) - f\int_O A_{H_2O}\otimes \exp^{-\frac{f}{p}t}dt - V_B\cdot R_{Hct}\int_O A_{O_2}dt}{f\int_O A_{O_2}\otimes \exp^{-\frac{f}{p}t}dt - V_B\cdot R_{Hct}\cdot F_v\int_O A_{O_2}dt}\end{aligned} \quad (1)$$

In the equation above, p is the blood/tissue partition coefficient of water (assumed to be 0.8 ml/ml), R_{Hct} is the small-to-large vessel hematocrit ratio (assumed to be 0.85), and V_B is the CBV obtained from $C^{15}O$ scan, and F_v is the effective venous fraction (fixed to 0.835). Finally, OEF (E) was calculated voxel-by-voxel using the equation below:

$$E = \frac{\int_O Ci(t) - f\int_O A_{H_2O}\otimes \exp^{-\frac{f}{p}t}dt - V_B\cdot R_{Hct}\int_O A_{O_2}dt}{f\int_O A_{O_2}\otimes \exp^{-\frac{f}{p}t}dt - V_B\cdot R_{Hct}\cdot F_v\int_O A_{O_2}dt} \quad (2)$$

In our DARG protocol, summation times of $^{15}O_2$ phase and $C^{15}O_2$ phase were 0–240 and 340–440 s, respectively.

Count-based OEF image

The ratio image defined as cbOEF image was defined as voxel-by-voxel ratio image of PET counts during $^{15}O_2$ phase and $C^{15}O_2$ phase. To investigate the optimal summation time for computing cbOEF against qOEF, we varied the summation time as 0–60, 0–120, 0–180, 0–240, 60–120, 60–180, 60–240, 120–180, 120–240, 180–240 s for $^{15}O_2$ phase, and 340–390, 390–440, 340–440 s for $C^{15}O_2$ phase. Therefore, the number of cbOEF images was total 30 for each subject.

Comparison of qOEF and cbOEF

In order to compare between cbOEF and qOEF, we calculate asymmetric index (AI) defined as $OEF_{vascular\ lesion\ site}/OEF_{normal\ site}$. As shown in Fig. 2, elliptic regions of interest (ROIs) (10 × 30 pixels) were drawn on 14 slices of vascular lesion site and normal site. The ROIs on the lesion site and the normal site were symmetric and there are total 28 ROIs. The all ROIs were drown on the qOEF image and superimposed to cbOEF image for each subject. The mean values within the ROIs were computed for the vascular lesion site and normal site, and the AI values for qOEF (qOEF-AI) and cbOEF (cbOEF-AI) with different summation times (total 30 patterns) were obtained. The slope of regression lines and coefficients of correlation between cbOEF-AI and qOEF-AI were calculated.

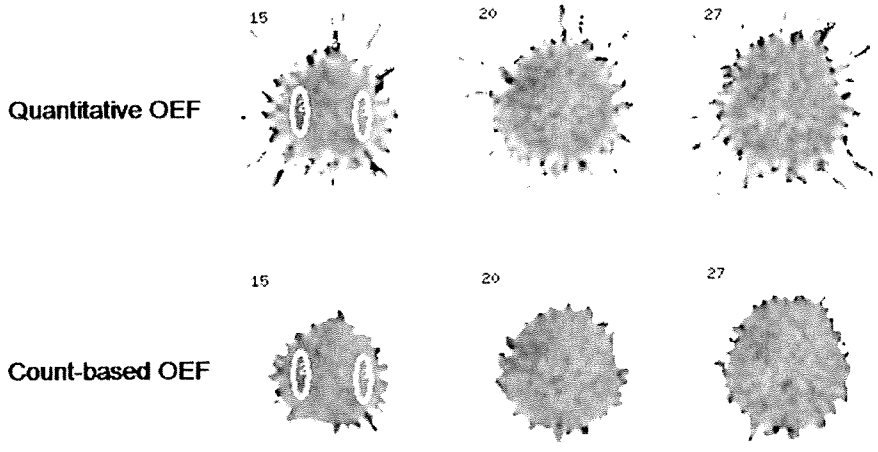

Fig. 2 This figure shows quantitative OEF images (*top*) and count-based OEF image ($^{15}O_2$ summation times 60–180 s, $C^{15}O_2$ summation time 340–440 s) (*down*) obtained on DARG method. The color scale of these images is relatively matched by normalizing maximum value of each OEF image. Ellipses in the qOEF and cbOEF images are ROIs. The size of ROIs was 10 × 30 pixels

Results

As shown in Fig. 2, cbOEF image from DARG protocol has similar image contrast against qOEF image, and better image quality (less noisy and no image artifact outside of the brain) than qOEF image. Comparisons between cbOEF-AI and qOEF-AI were carried out (Fig. 3), and correlation coefficient and slope of the regression line were summarized in Table 1. All plots except cbOEF-AI from 0 to 60 s of $^{15}O_2$ summed image have significant correlation ($P < 0.01$) against qOEF-AI. The best correlation coefficient was obtained as 0.94 when cbOEF was calculated from 0 to 180 s of $^{15}O_2$ summed image and 340–440 s of $C^{15}O_2$ summed image. However, the slope of the regression line in this case was 0.80, and cbOEF underestimated AI compared with qOEF. The slope of the regression almost became unity when cbOEF was calculated from 60 to 180 s of $^{15}O_2$ summed image and 340–390 s of $C^{15}O_2$ summed image.

Discussion

In this study, we investigated the relationship between cbOEF-AI and qOEF-AI obtained from the DARG protocol. The regression analysis was performed in order to optimize the summation time for $^{15}O_2$ phase and $C^{15}O_2$ phase in cbOEF calculation. By selecting the proper summation time, the cbOEF-AI could be utilized for diagnosing unilateral misery perfusion without arterial blood sampling.

The cbOEF image has been widely used with ^{15}O PET studies due to the simple calculation. Owing to this simplicity, the image quality of cbOEF is better than that of qOEF as shown in Fig. 2. However, since the cbOEF is empirical, in order to use the cbOEF as diagnostic tool, one must take into account of several factors such as radioactivity from blood vessel and recirculation water converted from $^{15}O_2$. The DARG protocol has another factor to be considered. Since the $C^{15}O_2$ gas is inhaled shortly after the $^{15}O_2$ gas inhalation in the DARG protocol, the residual radioactivity from $^{15}O_2$ gas and recirculation water converted from $^{15}O_2$ gas contaminates PET counts during $C^{15}O_2$ phase.

In order to interpret the results of Fig. 3 and Table 1, not only considering count statistics, it is important to consider the physiologic model of $^{15}O_2$ and water. As Mintun et al. proposed [13] that the total radioactivity in the tissue after the $^{15}O_2$ and $C^{15}O_2$ administration can be expressed as,

$$Ci(t) = f \cdot A_{H_2O}(t) \otimes \exp^{-\frac{f}{P}t} + E \cdot f \cdot A_{O_2}(t) \otimes \exp^{-\frac{f}{P}t} + V_B \cdot R_{Hct}(1 - F_v \cdot E)A_{O_2}(t) \quad (3)$$

The first term of the right-hand side describes the amount of water entering the tissue. The second term represents the amount of oxygen that enters the tissue and is immediately metabolized to water. The third term is the radioactivity of the $^{15}O_2$ in the blood vessels. After the inhalation of $^{15}O_2$ gas, the $^{15}O_2$ was metabolized in whole body as time advances, and the radioactivity of recirculation water gradually increases as the first term of the right-hand side of the Eq. 3. In general, the more the radioactivity from the recirculation water contains in the O_2 phase, the worse the cbOEF-AI correlates against qOEF-AI. As shown in Fig. 3 and Table 1, $^{15}O_2$ summation time extended to 240 s resulted in worse correlation than summation time to 180 s due to the influence of the recirculation water. If one compares between the results of the $C^{15}O_2$ summation time of 340–390 s (A) and 390–440 s (B), the slopes of (B) were smaller than (A) although the correlation coefficients for (B) were better than (A) in most cases. The count statistics of (B) was better than (A), which lead better correlation between cbOEF-AI and qOEF-AI. On the other hand, the $C^{15}O_2$ image of (B) has less contrast than (C) due to the diffusability of water, which causes the underestimation of cbOEF-AI against qOEF-AI. Because the $^{15}O_2$ image with the summation time of 0–60 s has the poorest count statistics, the cbOEF-AI with $^{15}O_2$ the summation time of 0–60 s had the worst correlation against qOEF-AI. Note that the blood component (the third term of Eq. 3) has the large influence on the $^{15}O_2$ image with summation time of 0–60 s, and the magnitude of this influence depends on the OEF value, which leads the underestimation of cbOEF-AI against qOEF-AI. Meanwhile, as judged by the best correlation coefficient, we recommend to use the following combinations:

- $^{15}O_2$ summation time of 0–180 s and $C^{15}O_2$ summation time of 340–440 s
- $^{15}O_2$ summation time of 60–180 s and $C^{15}O_2$ summation time of 340–390 s

In the latter case, the correlation coefficient was lower than one in the former, but this combination makes it possible to shorten the PET acquisition time.

Kobayashi et al. [25] reported the cbOEF-AI can be successfully used to diagnose misery perfusion if one uses 4–7 min of the summation time for continuous inhalation of $^{15}O_2$ gas in addition to 3 min of $H_2^{15}O$ PET acquisition. In their study, the waiting time between $^{15}O_2$ scan and $H_2^{15}O$ scan is necessary to avoid contamination of $^{15}O_2$ radioactivity in $H_2^{15}O$ data. Hence, the total study time for their study should be longer than 10 min. As shown in this paper, the qOEF-AI equivalent cbOEF-AI will be able to be obtained by 7.3 min after the start of $^{15}O_2$ inhalation. By using cbOEF-AI with the DARG protocol, total study time can be dramatically shortened, which is beneficial for patients as well as medical staff, and the cbOEF-AI with

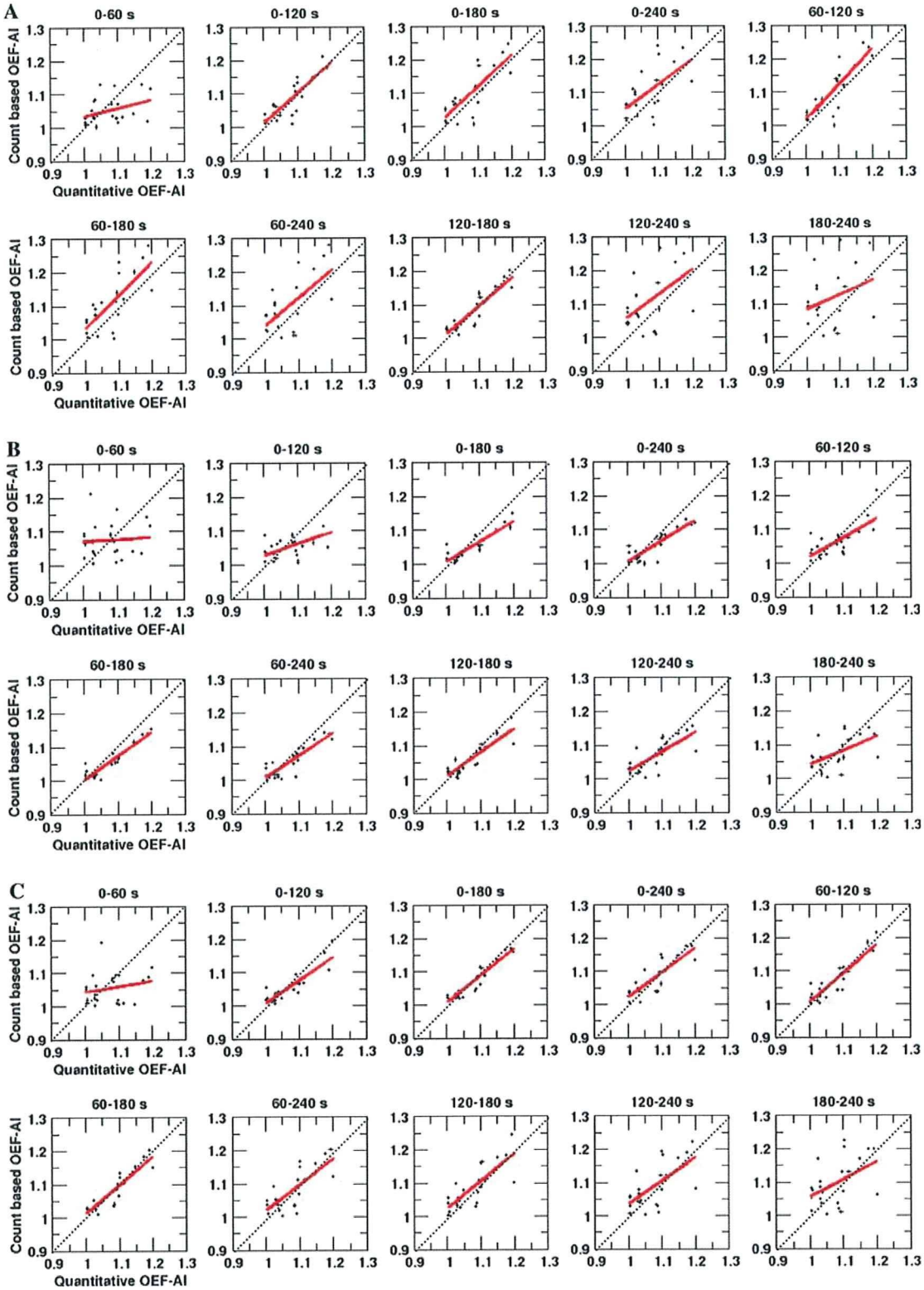

Fig. 3 These graphs show the correlation between qOEF-AI and cbOEF-AI. Each graph has different summation time for $^{15}O_2$ and $C^{15}O_2$ phases in the DARG protocol. The title of each graph represents the summation time for $^{15}O_2$ phase. The summation times for $C^{15}O_2$ phase are from 340 to 390 s for (**a**), 390–440 s for (**b**), and 340–440 s for (**c**)

Table 1 Correlation coefficient, slope and *y*-intercept between qOEF-AI and cbOEF-AI with different summation periods

O_2 summation time (s)	CO_2 summation time (s)								
	340–390 (A)			390–440 (B)			340–440 (C)		
	Correlation coefficient	Slope	*y*-Intercept	Correlation coefficient	Slope	*y*-Intercept	Correlation coefficient	Slope	*y*-Intercept
0–60	0.35	0.24	0.79	0.06	0.05	1.02	0.21	0.16	0.88
0–120	0.87	0.91	0.10	0.52	0.35	0.68	0.88	0.69	0.31
0–180	0.79	0.94	0.09	0.90	0.59	0.41	0.94	0.80	0.20
0–240	0.59	0.74	0.30	0.86	0.61	0.39	0.83	0.74	0.28
60–120	0.84	1.06	−0.05	0.74	0.57	0.44	0.90	0.87	0.13
60–180	0.75	0.99	0.04	0.93	0.70	0.29	0.91	0.86	0.15
60–240	0.63	0.84	0.19	0.87	0.66	0.34	0.77	0.78	0.24
120–180	0.91	0.86	0.15	0.89	0.70	0.30	0.79	0.82	0.20
120–240	0.51	0.73	0.23	0.75	0.59	0.43	0.64	0.70	0.20
180–240	0.30	0.44	0.64	0.54	0.42	0.61	0.47	0.54	0.51

Time 0 was the $^{15}O_2$ scan start time. The scan for $^{15}O_2$ and $C^{15}O_2$ was the single scan for 480 s

the DARG protocol might be used for acute patients due to its simple and rapid procedure.

As shown in Fig. 1, even though the DARG protocol can be terminated at 7.3 min from $^{15}O_2$ inhalation, our study must have 10 min of transmission scan to correct attenuation of photons. The time duration for the transmission scan is possible to minimized by segmented attenuation correction techniques [28], or using hybrid PET-CT scanner. Note that for computing cbOEF-AI, no $C^{15}O$ scan is required. Kobayashi et al. [24] showed no blood volume correction was required to compute cbOEF-AI, when they used bolus injection of $H_2^{15}O$ instead of steady-state protocol.

In this study, we used the DARG protocol with $C^{15}O_2$ inhalation after 6 min from the beginning of $^{15}O_2$ inhalation. The optimal summation time for cbOEF-AI could be different if the time interval between inhalations of $^{15}O_2$ and $C^{15}O_2$ gases is altered. If one is administrated $C^{15}O_2$ gas earlier than 6 min, the contamination of $^{15}O_2$ radioactivity on $C^{15}O_2$ phase becomes larger, which will result in changing optimal summation time for cbOEF-AI. Further systematic investigations will be required to obtain more general conclusion, and it might be possible to shorten the total scan duration for proper cbOEF-AI with the DARG protocol. The image quality of PET is also influenced on the results. In our study, all data were obtained in 2D mode. It is not clear that 3D acquisition of PET affects our results. Ibaraki et al showed that qOEF was possible to obtain in 3D acquisition as good as 2D acquisition [29], which suggests the usability of cbOEF in 3D acquisition, although further studies are required to confirm. For computing cbOEF, it is important to assure that a patient does not move during PET acquisition. There are several techniques to compensate the motion of the patient by means of hardware [30] or software although simplicity of cbOEF-AI is lost by applying these techniques. We blindly selected data from patients, who underwent DARG protocol. Therefore, varieties of patient's history and diagnosis were included, and it is difficult to judge clinical usability of the cbOEF-AI with DARG protocol by our study so far. Clinical impact of cbOEF-AI with DARG protocol is beyond the scope of this paper. We have a plan to evaluate diagnostic accuracy for the present technique in future.

Conclusion

In this paper, we investigated the feasibility of cbOEF-AI with DARG protocol, and relationship between cbOEF-AI and qOEF-AI by varying the summation time. The cbOEF-AI with the DARG protocol may contribute to diagnose unilateral misery perfusion within 7.3 min.

References

1. Powers WJ. Cerebral hemodynamics in ischemic cerebrovascular disease. Ann Neurol. 1991;29:231–40. doi:10.1002/ana.410290302.
2. Baron JC, Bousser MG, Rey A, Guillard A, Comar D, Castaigne P. Reversal of focal "misery-perfusion syndrome" by extra-intracranial arterial bypass in hemodynamic cerebral ischemia: a case study with ^{15}O positron emission tomography. Stroke. 1981;12:454–9.
3. Yamauchi H, Fukuyama H, Nagahama Y, Nabatame H, Nakamura K, Yamamoto Y, et al. Evidence of misery perfusion and risk for recurrent stroke in major cerebral arterial occlusive diseases from PET. J Neurol Neurosurg Psychiatry. 1996;61:18–25. doi:10.1136/jnnp.61.1.18.
4. Yamauchi H, Fukuyama H, Nagahama Y, Nabatame H, Ueno M, Nishizawa S, et al. Significance of increased oxygen extraction

fraction in 5-year prognosis of major cerebral arterial occlusive disease. J Nucl Med. 1999;40:1992–8.
5. Grubb RL Jr, Derdeyn CP, Fritsch SM, Carpenter DA, Yundt KD, Videen TO, et al. Importance of hemodynamic factors in the prognosis of symptomatic carotid occlusion. JAMA. 1998;280: 1055–60. doi:10.1001/jama.280.12.1055.
6. Derdeyn CP, Grubb RL Jr, Powers WJ. Cerebral hemodynamic impairment: method of measurement and association with stroke risk. Neurology. 1999;53:251–9.
7. Derdeyn CP, Videen TO, Yundt KD, Fritsch SM, Carpernter DA, Grubb RL Jr, et al. Variability of cerebral blood volume and oxygen extraction: stage of erebral hemodynamic impairment revisited. Brain. 2002;125:595–607. doi:10.1093/brain/awf047.
8. Subramanyam R, Alpert NM, Hoop B Jr, Brownell GL, Yaveras JM. A model for regional cerebral oxygen distribution during continuous inhalation of $^{15}O_2$, $C^{15}O$, and $C^{15}O_2$. J Nucl Med. 1978;19:48–53.
9. Lammertsma AA, Heather JD, Jones T, Frackowiak RS, Lenzi GL. A statistical study of the steady state technique for measuring regional cerebral blood flow and oxygen utilization using ^{15}O. J Comput Assist Tomogr. 1982;6:566–73. doi:10.1097/00004728-198206000-00022.
10. Correia JA, Alpert NM, Buxton RB, Ackerman RH. Analysis of some errors in the measurement of oxygen extraction and oxygen consumption by the equilibrium inhalation method. J Cereb Blood Metab. 1985;5:591–9.
11. Okazawa H, Yamauchi H, Sugimoto K, Takahashi M, Toyoda H, Kishibe Y, et al. Quantitative comparison of the bolus and steady-state methods for measurement of cerebral perfusion and oxygen metabolism: positron emission tomography study using ^{15}O-gas and water. J Cereb Blood Metab. 2001;21:793–803. doi: 10.1097/00004647-200107000-00004.
12. Okazawa H, Yamauchi H, Sugimoto K, Toyoda H, Kishibe Y, Takahashi M. Effects of acetazolamide on cerebral blood flow, blood volume, and oxygen metabolism: a positron emission tomography study with healthy volunteers. J Cereb Blood Flow Metab. 2001;21:1472–9. doi:10.1097/00004647-200112000-00012.
13. Mintun MA, Raichle ME, Martin WR, Herscovitch P. Brain oxygen utilization measured with O-15 radiotracers and positron emission tomography. J Nucl Med. 1984;25(2):177–87.
14. Iida H, Jones T, Miura S. Modeling approach to eliminate the need to separate arterial plasma in oxygen-15 inhalation positron emission tomography. J Nucl Med. 1993;34:1333–40.
15. Sadato N, Yonekura Y, Senda M, Iwasaki Y, Matoba N, Tamaki N, et al. PET and the autoradiographic method with continuous inhalation of oxygen-15-gas: theoretical analysis and comparison with conventional steady-state methods. J Nucl Med. 1993;34: 1672–80.
16. Hatazawa J, Fujita H, Kanno I, Satoh T, Iida H, Miura S, et al. Regional cerebral blood flow, blood volume, oxygen extraction fraction, and oxygen utilization rate in normal volunteers measured by the autoradiographic technique and the single breath inhalation method. Ann Nucl Med. 1995;9:15–21.
17. Shidahara M, Watabe H, Kim KM, Oka H, Sago M, Hayashi T, et al. Evaluation of a commercial PET tomograph-based system for the quantitative assessment of rCBF, rOEF and $rCMRO_2$ by using sequential administration of ^{15}O-labeled compounds. Ann Nucl Med. 2002;16(5):317–27. doi:10.1007/BF02988616.
18. Hattori N, Bergsneider M, Wu HM, Glenn TC, Vespa PM, Hovda DA, et al. Accuracy of a method using short inhalation of ^{15}O–O_2 for measuring cerebral oxygen extraction fraction with PET in healthy humans. J Nucl Med. 2004;45:765–70.
19. Kudomi N, Hayashi T, Teramoto N, Watabe H, Kawachi N, Ohta Y, et al. Rapid quantitative measurement of $CMRO_2$ and CBF by dual administration ^{15}O-labeled oxygen and water during a single PET scan—a validation study and error analysis in anesthetized monkeys. J Cereb Blood Flow Metab. 2005;25:1209–24. doi: 10.1038/sj.jcbfm.9600118.
20. Jone T, Chesler DA, Ter-Pogossian MM. The continuous inhalation of oxygen-15 for assessing regional oxygen extraction in the brain of man. Br J Radiol. 1976;49:339–43.
21. Derdeyn CP, Videen TO, Simmons NR, Yundt KD, Fritsch SM, Grubb RL Jr, et al. Count-based PET method for predicting ischemic stroke in patients with symptomatic carotid arterial occlusion. Radiology. 1999;212:499–506.
22. Derdeyn CP, Videen TO, Grubb RL Jr, Powers WJ. Comparison of PET oxygen extraction fraction method for the prediction of stroke risk. J Nucl Med. 2001;42(8):1195–7.
23. Ibaraki M, Shimosegawa E, Miura S, Takahashi K, Ito H, Kanno I, et al. PET measurements of CBF, OEF, and $CMRO_2$ without arterial sampling in hyperacute ischemic stroke: method and error analysis. Ann Nucl Med. 2004;18:35–44. doi:10.1007/BF02985612.
24. Kobayashi M, Okazawa H, Tsuchida T, Kawai K, Fujibayashi Y, Yoneyama Y. Diagnosis of misery perfusion using noninvasive ^{15}O-gas PET. J Nucl Med. 2006;47:1581–6.
25. Kobayashi M, Kudo T, Tsujikawa T, Isozaki M, Araki Y, Fujibayashi Y, et al. Shorter examination method for the diagnosis of misery perfusion with count-based oxygen extraction fraction elevation in ^{15}O-gas PET. J Nucl Med. 2008;49:242–6. doi: 10.2967/jnumed.107.047118.
26. Kudomi N, Choi E, Yamamoto S, Watabe H, Kim KM, Shidahara M, et al. Development of a GSO detector assembly for a continuous blood sampling system. IEEE Trans Nucl Sci. 2003; 50(1):70–3. doi:10.1109/TNS.2002.807869.
27. Kudomi N, Watabe H, Hayashi T, Iida H. Separation of input function for rapid measurement of quantitative $CMRO_2$ and CBF in a single PET scan with a dual tracer administration method. Phys Med Biol. 2007;52(7):1893–908. doi:10.1088/0031-9155/52/7/009.
28. Xu M, Cutler PD, Luk WK. Adaptive, segmented attenuation correction for whole-body PET imaging. IEEE Trans Nucl Sci. 1996;43:331–6. doi:10.1109/23.485974.
29. Ibaraki M, Miura S, Shimosegawa E, Sugawara S, Mizuta T, Ishikawa A, et al. Quantification of cerebral blood flow and oxygen metabolism with 3-dimensional PET and ^{15}O: validation by comparison with 2-dimensional PET. J Nucl Med. 2007;49: 50–9. doi:10.2967/jnumed.107.044008.
30. Woo SK, Watabe H, Choi Y, Kim KM, Park CC, Bloomfield PM, et al. Sinogram-based motion correction of PET images using optical motion tracking system and list-mode data acquisition. IEEE Trans Nucl Sci. 2004;51(3):782–8. doi:10.1109/TNS.2004.829786.

3-Tesla Magnetic Resonance Angiographic Assessment of a Tissue-Engineered Small-Caliber Vascular Graft Implanted in a Rat

Masashi Yamanami,[1,2] Akihide Yamamoto,[3,4] Hidehiro Iida,[3,4] Taiji Watanabe,[1,2] Keiichi Kanda,[2] Hitoshi Yaku,[2] Yasuhide Nakayama[1]

[1] Department of Bioengineering, Advanced Biomedical Engineering Center, National Cardiovascular Center Research Institute, Osaka, Japan

[2] Department of Cardiovascular Surgery, Kyoto Prefectural University of Medicine, Kyoto, Japan

[3] Department of Investigative Radiology, Advanced Biomedical Engineering Center, National Cardiovascular Center Research Institute, Osaka, Japan

[4] Department of Medical Physics and Engineering, Division of Health Sciences, Graduate School of Medicine, Osaka University, Osaka, Japan

Received 30 January 2009; revised 4 June 2009; accepted 15 July 2009
Published online 2 October 2009 in Wiley InterScience (www.interscience.wiley.com). DOI: 10.1002/jbm.b.31501

Abstract: In the development of small-caliber vascular grafts (diameter; less than 3 mm), animal implantation studies have been mostly performed by using rat abdominal aortas, and their certain patency must evaluate with sacrificing every observation periods, which is both labor-intensive and time-consuming when performing a large number of experiments. This study is the first to demonstrate the application of 3-Tesla contrast-free time-of-flight magnetic resonance angiography (TOF-MRA) in the continuous assessment of the status of a tissue-engineered vascular graft in rat. As a model graft, a single connective tubular tissue (diameter; 1.5 mm), prepared by embedding the silicone rod (diameter; 1.5 mm) into a subcutaneous pouch of a rat for 2 weeks an *in vivo* tissue-engineering, was used. The graft was implanted in the abdominal aorta (diameter; 1.3 mm) of the rat by end-to-end anastomosis. Repeated TOF-MRA imaging of the graft obtained over a 3-month follow-up period after implantation made it possible to evaluate the patency of the graft, both simply and noninvasively. It also permitted visualization of the connected abdominal aorta and renal and common iliac arteries having smaller caliber (diameter; less than 1 mm). In addition, the degree of the stenosis or aneurysm could also be detected. 3-Tesla MRA allowed the simplified and noninvasive assessment of the status on the vascular graft, including the formation of a stenosis or aneurysm, in the same rat at different times, which will be contributing to enhance the development of tissue-engineered vascular grafts even with small caliber. © 2009 Wiley Periodicals, Inc. J Biomed Mater Res Part B: Appl Biomater 92B: 156–160, 2010

Keywords: small-caliber vascular grafts; magnetic resonance angiography; animal implantation; biotube; tissue engineering

INTRODUCTION

Small-caliber arterial substitutes are needed for cardiac and peripheral revascularization procedures. For such small artery bypass grafting procedures, autologous arterial (e.g., internal thoracic artery and radial artery) or venous (e.g., saphenous vein) grafts still remain the most ideal vascular substitutes.[1,2] However, many patients do not have a vessel suitable for use owing to the poor quality, inadequate size or length, or previous harvest of such vessels. Moreover, a second surgical procedure is required to initially obtain the necessary vessel. Vascular prostheses, such as expanded polytetrafluoroethylene (ePTFE) and poly (ethylene terephthalate) (Dacron) grafts, have been used clinically for reconstructing arteries.[3] However, small-caliber (<6 mm) arterial substitutes have generally proved inadequate largely because of the formation of thromboses and intimal hyperplasia.[4,5]

Many design criteria have been proposed for the development of functional small-caliber arterial replacement grafts.[5–11] All most of all artificial vascular grafts (inner diameter, 1.5–3.0 mm) have been employed for transplantation

Correspondence to: Y. Nakayama (e-mail: nakayama@ri.ncvc.go.jp)

to rat abdominal aortas as an *in vivo* model.[6–8] Graft patency has been evaluated during the follow-up period by angiography[8] or by direct inspection at the time of removal for histological evaluation.[6,7] However, angiography requires cannulation of the carotid artery,[8] and a midline laparotomy is needed for direct inspection.[6,7] As a consequence, these methods are complex and invasive. Therefore, it is difficult to evaluate graft patency repeatedly in the same rat. Although, graft patency has also been evaluated by palpating the femoral pulse,[7] this method is subjective and uncertain.

The current imaging systems, including fluorescence antibody method, single photon emission computed tomography (SPECT),[12] laser doppler system,[13] or high-resolution ultrasound[14] for blood flow imaging in addition to magnetic resonance angiography (MRA), are powerful tool in tissue engineering field. However, it is considered that no imaging systems except for MRA fit for evaluation of the status of implanted small-caliber vascular grafts.

In clinical practice, MRI has been used as a noninvasive evaluation method for the assessment of brain blood vessels and peripheral arteries and also been widely used in preclinical research on experimental small rodents.[15–18] The studies have typically been aimed at understanding the patho-physiological status and evaluating the efficacy/side effects of newly developed treatments, such as pharmaceutical and regenerative medicine.

Our purpose in this study was to evaluate the status of a tissue-engineered vascular graft with inner diameter of 1.5 mm, clinically, repeatedly, and noninvasively in a rat implantation model. To this end, 3-Tesla contrast-free time-of-flight magnetic resonance angiography (TOF-MRA) was applied.

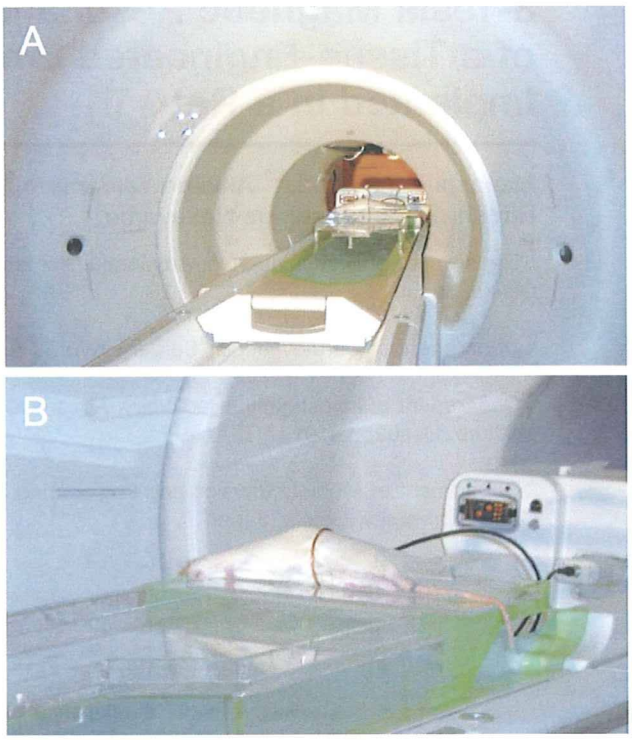

Figure 1. Experimental setup in MR imaging on a human whole-body 3T-MR scanner (GE Healthcare) (A). The coil was placed at the center of the gantry and its turn axis had perpendicular alignment to the static magnetic field (B). Rat's abdomen was positioned inside the coil along the craniocaudal direction. [Color figure can be viewed in the online issue, which is available at www.interscience.wiley.com.]

MATERIALS AND METHODS

Preparation and Implantation of the Connective Tubular Tissue

All animal experiments were conducted in accordance with local regulations, complying with the Principles of Laboratory Animal Care (formulated by the National Society for Medical Research) and the Guide for the Care and Use of Laboratory Animals (NIH Publication No. 86–23, revised 1985). The research protocol (No. 8050) was approved by the ethics committee of the National Cardiovascular Center Research Institute.

The connective tubular tissue was prepared by *in vivo* tissue engineering according to the previous reported method.[9] Briefly, a silicone rod (diameter, 1.5 mm; length, 10 mm; Tigers Polymer, Osaka, Japan) was used as a mold. One adult female Wistar rat (weight; 300 g) was anesthetized with 1.5% isoflurane (vol/vol air). The mold was placed in a dorsal subcutaneous pouch, and after 2 weeks, the implant was removed. The tubular tissue was obtained from the implant after trimming the peripheral tissues and pulling out the rod. The tube thus obtained was treated by coating with Argatroban (1 mg/graft; Mitsubishi Chemical Co., Tokyo, Japan) to make it antithrombogenic. It was then implanted to the infrarenal abdominal aorta of the same rat using an end-to-end anastomosis under microscopic guidance and sutured using 12 interrupted 10–0 nylon stitches [Figure 1(A)]. Patency was examined at the time of surgery by direct inspection. The wound was closed with 4–0 silk sutures. Thereafter, the rat had free access to standard food and water. Graft status was evaluated at 2, 36, and 78 days after transplantation by contrast-free TOF-MRA under anesthesia induced by an intramuscular injection of pentobarbital (40 mg/kg).

MR Data Acqusition

A human whole-body 3-Tesla magnetic resonance imaging (MRI) scanner (Signa, GE Healthcare, Milwaukee, WI) was employed in this study (Figure 1). The gradient coil system was capable of providing a maximum gradient amplitude of 40 mT/m. All sequence programs employed in this study were designed for clinical studies. A developed single-turn surface coil of 62 mm diameter was used for MR imaging [Figure 1(B)]. Contrast-free TOF-MRA was performed using a three-dimensional flow-compensated fast spoiled gradient recalled (3D-FSPGR) sequence [repetition

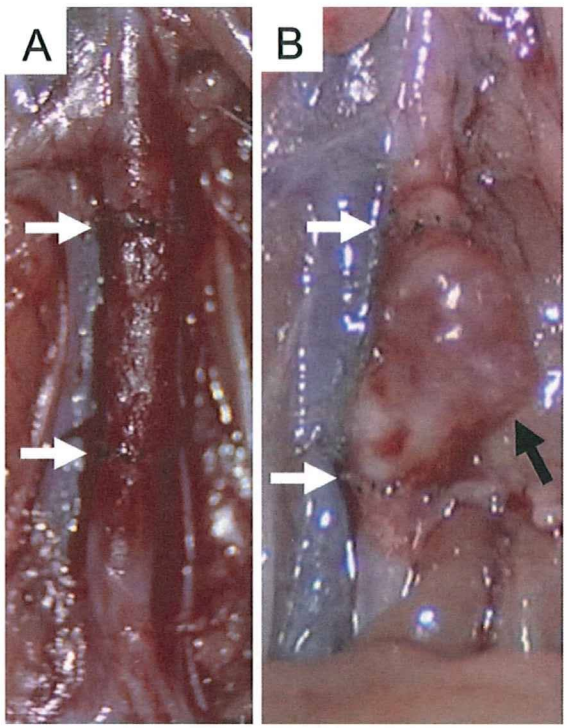

Figure 2. (A) The tubular connective tissue vascular graft (diameter; 1.5 mm) after autoimplantation in the rat infrarenal abdominal aorta (diameter; 1.3 mm) performed by end-to-end anastomosis under microscopic guidance using 12 interrupted stitches of 10-0 nylon suture. (B) The tubular connective tissue formed an aneurysm (max diameter; 3.0 mm) at 78 days after autoimplantation. White arrows indicate the proximal and distal anastomosis regions. Black arrow indicates the aneurysm. [Color figure can be viewed in the online issue, which is available at www.interscience.wiley.com.]

time (TR) = 21 ms, echo time (TE) = 5.4 ms (out of phase), flip angle (FA) = 15°, slice thickness = 0.4 mm, field of view (FOV) = 80 mm × 60 mm, matrix = 288 × 192, locs per slab = 128, the number of excitations (NEX) = 1, scanning time = 5 min 58 s]. For suppressing venous signals, a region of 40-mm thickness on the caudal side of the measured slab was saturated. The measured voxel size in TOF-MRA was 0.278 × 0.291 × 0.400 mm. The image reconstruction was zero-filled to a matrix size of 512 × 512 and the voxel size was 0.156 × 0.156 × 0.400 mm. MR angiograms were analyzed by generating the partial maximum intensity projection (pMIP) with a commercial software package (AZE, Tokyo, Japan). Our previous report on TOF-MRA was shown detail in rat.[13]

RESULTS

The tubular connective tissue with a diameter of 1.5 mm was autoimplanted successfully into the 1.3 mm diameter abdominal aorta of the rat by end-to-end anastomosis [Figure 2(A)]. After suturing with 12 interrupted stitches, there was little bleeding from either of the sites of anastomosis, indicated by the arrows in Figure 2(A). The patency of the graft was recognized directly by the satisfactory pulsation at the graft and distal side of the aorta.

3-Tesla contrast-free TOF-MRA of the rat was performed at 2 days after implantation [Figure 3(A)] to evaluate the status of the graft. The measurement time was ~6 min and no contrast medium was needed. The MRA distinctly visualized the patent graft connected to the abdominal aorta together with renal arteries and common iliac arteries of 0.7 and 0.8 mm diameter, respectively. Spatial resolution in the MRA was less than several hundred microns. A mechanical stenotic lesion, which may have been due to the anastomosis, was observed in both anastomosis regions. At 36 days after implantation, little stenosis and no aneurismal dilation of the graft were observed [Figure 3(B)]. At 78 days after implantation, the maximum diameter of the aneurysm formed at the graft was 3.0 mm [Figure 3(C)]. The shape of the aneurysm was very close to that observed macroscopically [Figure 2(B)]. Therefore, the status of the graft could be precisely determined, repeatedly, and noninvasively.

DISCUSSION

This study is the first to demonstrate the application of MRA to the evaluation of the status of a small-caliber arti-

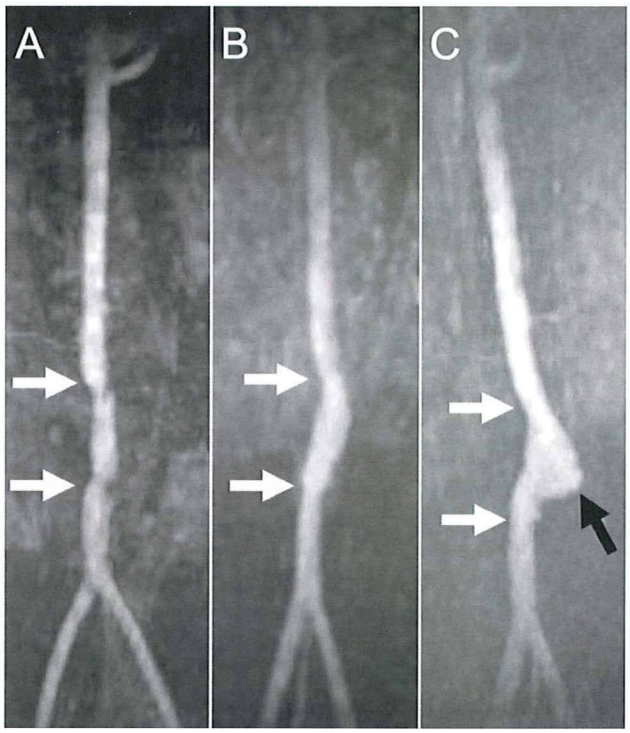

Figure 3. 3-Tesla contrast-free TOF-MRA images of the rat abdominal aorta at 2 (A), 36 (B), and 78 (C) days after autoimplantation of the biotube vascular graft. White arrows indicate the proximal and distal anastomosis regions of the abdominal aorta. A stenotic lesion was visible in the anastomosis regions at 2 days. An aneurysm formation in the graft was visible at 78 days (black arrow indicates the aneurysm).

ficial vascular graft implanted in the abdominal aorta of a rat. In the development of small-caliber vascular grafts as a preclinical study, *in vivo* evaluation is needed. Implantation studies have been performed mostly by using the abdominal aorta of rats.[6–8] Their certain patency must evaluate with sacrificing every observation periods, which is both labor-intensive and time-consuming when performing a large number of experiments. Since some rats survive with no symptoms after graft occlusion, assessment of the occlusion of an abdominal aorta after graft implantation is not possible solely on the basis of the rat's appearance. On the other hand, some researchers have evaluated graft patency by palpating the femoral pulse[7]; however, this method is prone to subjectivity and uncertainty. Therefore, evaluation of graft patency should be performed by direct inspection under laparotomy. On the other hand, even in histological observations, the evaluation of the degree of graft stenosis is very difficult.

In this study, MRI images of a reasonable quality were obtained from a rat using a human whole-body MRI scanner at 3-Tesla. Contrast-free TOF-MRA was able to depict the implanted graft with a diameter of ~1.5 mm, connected to the abdominal aorta with a diameter of ~1.3 mm, and also revealed arteries with diameters of less than 1 mm, such as the renal, common iliac, and tail arteries. In addition, an evaluation of the graft status, including the stenosis, was also feasible due to the high resolution and reasonable contrast. As indicated in Figure 3(A), the mechanical stenosis was clearly indicated at both sites of anastomosis. Furthermore, the aneurysm formation was clearly observed [Figure 3(C)]. Since the observation by MRA is simple and noninvasive, assessment of the status of small-caliber vascular grafts could be performed in the same rat at different times. The repeatable MRA observation in a single rat enabled correct assessment of the graft status over the follow-up period. Such repeatability will reduce the variation in results stemming from individual difference in experimental animals.

As a model graft for implantation in this study, the tubular connective tissue was used. The tissue was prepared similar to biotubes.[9] Biotubes are autologous prosthetic tubular tissues prepared by in-body tissue architecture technology. The biotube, obtained from rats by embedding the silicone rods (diameter; 3 mm) into their subcutaneous pouches for 4 weeks, had several 10 μm in thickness, about 500 gf in maximum load at rapture, and about 1000 mmHg in burst pressure.[19] This technology, a novel and practical concept in regenerative medicine, is based on the phenomenon of tissue encapsulation of foreign materials *in vivo*, and it can be used to develop autologous tissues of the desired shape, depending on the mold design.[9–11] Using this technology, several types of tissues, including "biotubes" as vascular tissues,[9–11] "biovalves" as tri-leaflet heart valve-shaped tissues,[20,21] and "biocovered stents" as hybrid IVR devices,[22] have been developed. In this study, by shortening of the encupsulation period weak and ununiform wall structure was prepared particularly for observation of the variety of vascular graft fate. As expected, normal, stenosis, or aneurysm models were appropriately obtained in one rat.

The assessment of graft status using MR imaging does, however, have limitations. When using certain materials for artificial grafts (e.g., ePTFE and Dacron), MR imaging might be difficult owing to graft artifacts. Furthermore, such as ultrasound and/or digital subtraction angiography, it is difficult to evaluate blood stream by 3D evaluation. The TOF-MRA is more appropriate for the evaluation of tissue-engineered vascular grafts. The signal-to-noise ratio in image quality on TOF-MRA is strongly dependent on the static field strength and the coil design. Further study should be needed in developing coil. We hope that others who study at understanding the patho-physiological status and evaluating the efficacy/side effects of newly developed treatments, such as pharmaceutical and regenerative medicine.

CONCLUSIONS

Contrast-free TOF-MRA with 3-Tesla allowed an assessment of tissue-engineered small-caliber vascular graft status in the rat systemic arterial circulation. As the protocol used in this study is simple and noninvasive, it is useful for the longitudinal evaluation of graft status in the rat; this will contribute to enhancing the development of tissue-engineered small-caliber vascular grafts, particularly in the field of regenerative medicine.

REFERENCES

1. Tomizawa Y. Vascular prostheses for aortocoronary bypass grafting: A review. Artif Organs 1995;19:39–45.
2. Ferrari ER, Von Segesser LK. Arterial grafting for myocardial revascularization: How better is it? Curr Opin Cardiol 2006; 21:584–588.
3. Zilla P, Bezuidenhout D, Human P. Prosthetic vascular grafts: Wrong models, wrong questions and no healing. Biomaterials 2007;28:5007–5027.
4. Pasquinelli G, Freyrie A, Preda P, Curti T, D'addato M, Laschi R. Healing of posthetic arterial grafts. Scanning Microsc 1990;4:351–362.
5. Isenberg BC, Williams C, Tranquillo RT. Small-diameter artificial arteries engineered in vitro. Circ Res 2006;98:25–35.
6. Doi K, Nakayama Y, Oka T, Matsuda T. A new microporous polyurethane vascular graft prepared by an excimer laser ablation technique. ASAIO J 1995;41:M608–M611.
7. Campbell JH, Efendy JE, Campbell GR. Novel vascular graft grown within recipient's own peritoneal cavity. Circ Res 1999; 85:1173–1178.
8. Pektok E, Nottelet B, Tille JC, Gurny R, Kalangos A, Moeller M, Walpoth BH. Degradation and healing characteristics of small-diameter poly (epsilon-caprolactone) vascular grafts in the rat systemic arterial circulation. Circulation 2008;118:2563–2570.
9. Nakayama Y, Ishibashi-Ueda H, Takamizawa K. In vivo tissue-engineered small-caliber arterial graft prosthesis consisting of autologous tissue (Biotube). Cell Transplant 2004;13: 439–449.

10. Sakai O, Kanda K, Ishibashi-Ueda H, Takamizawa K, Ametani A, Yaku H, Nakayama Y. Development of the wing-attached rod for acceleration of "Biotube" vascular grafts fabrication in vivo. J Biomed Mater Res B Appl Biomater 2007; 83:240–247.
11. Watanabe T, Kanda K, Ishibashi-Ueda H, Yaku H, Nakayama Y. Development of biotube vascular grafts incorporating cuffs for easy implantation. J Artif Organs 2007;10:10–15.
12. Kempen DH, Yaszemski MJ, Heijink A, Hefferan TE, Creemers LB, Britson J, Maran A, Classic KL, Dhert WJ, Lu L. Non-invasive monitoring of BMP-2 retention and bone formation in composites for bone tissue engineering using SPECT/CT and scintillation probes. J Control Release 2009; 134:169–176.
13. Hobo K, Shimizu T, Sekine H, Shin'oka T, Okano T, Kurosawa H. Therapeutic angiogenesis using tissue engineered human smooth muscle cell sheets. Arterioscler Thromb Vasc Biol 2008;28:637–643.
14. Mccarthy I. The physiology of bone blood flow: A review. J Bone Joint Surg Am 2006;88:4–9.
15. Brockmann MA, Kemmling A, Groden C. Current issues and perspectives in small rodent magnetic resonance imaging using clinical MRI scanners. Methods 2007;43:79–87.
16. Yamamoto A, Sato H, Enmi J, Ishida K, Ose T, Kimura A, Fujiwara H, Watabe H, Hayashi T, Iida H. Use of a clinical MRI scanner for preclinical research on rats. Radiol Phys Technol 2009;2:13–21.
17. Smith DA, Clarke LP, Fiedler JA, Murtagh FR, Bonaroti EA, Sengstock GJ, Arendash GW. Use of a clinical MR scanner for imaging the rat. Brain Res Bull 1993;31:115–120.
18. Guzman R, Lövblad KO, Meyer M, Spenger C, Schroth G, Widmer HR. Imaging the rat brain on a 1.5 T clinical MR-scanner. J Neurosci Methods 2000;97:77–85.
19. Huang H, Zhou YM, Ishibashi-Ueda H, Takamizawa K, Ando J, Kanda K, Yaku H, Nakayama Y. *In vitro maturation* of "Biotube" vascular grafts induced by a 2-day pulsatile flow loading. J Biomed Mater Res B Appl Biomater 2009 [Epub ahead of print].
20. Hayashida K, Kanda K, Yaku H, Ando J, Nakayama Y. Development of an in vivo tissue-engineered, autologous heart valve (the biovalve): Preparation of a prototype model. J Thorac Cardiovasc Surg 2007;134:152–159.
21. Hayashida K, Kanda K, Oie T, Okamoto Y, Sakai O, Watanabe T, Ishibashi-Ueda H, Onoyama M, Tajikawa T, Ohba K, Yaku H, Nakayama Y. "In vivo tissue-engineered" valved conduit with designed molds and laser processed scaffold. J Cardiovasc Nurs 2008;23:61–64.
22. Nakayama Y, Zhou YM, Ishibashi-Ueda H. Development of in vivo tissue-engineered autologous tissue-covered stents (biocovered stents). J Artif Organs 2007;10:171–176.

Conceptual Design of High Resolution and Quantitative SPECT System for Imaging a Selected Small ROI of human brain

Tsutomu Zeniya, Yoshiyuki Hirano, Tomonori Sakimoto, Kenji Ishida, Hiroshi Watabe, *Member, IEEE*, Noboru Teramoto, Hiroyuki Kudo, *Member, IEEE*, Kotaro Minato, *Member, IEEE*, Jun Hatazawa, and Hidehiro Iida, *Member, IEEE*

Abstract– **We designed a concept of high resolution and quantitative SPECT for imaging a selected small region-of-interest (ROI) of human brain. This system is aimed at achieving high resolution less than 1 mm and being applied for imaging neurons and evaluating drug delivery system. Pinhole or cone-beam collimators are useful for high-resolution imaging of small ROI. However, when the ROI is smaller than the object, the projection data are truncated by radioisotope outside ROI. In the reconstructed image, the truncation causes the artifact and the overestimation of voxel value, which deceases quantitative accuracy of physiological functions. We are introducing the new truncation compensated 3D-OSEM (TC-3DOSEM) reconstruction method. The truncated data can be successfully reconstructed within ROI by fulfilling the condition that ROI contains a priori knowledge. In addition to small field-of-view (FOV) detector, we are introducing the parallel-hole collimator attached large FOV detector covering the entire brain, to acquire the non-truncated data and provide the priori knowledge in small ROI, even if the resolution of the detector is low. For imaging with high resolution, we are using $LaBr_3$(Ce) scintilator with optically coupled to position-sensitive photomultiplier tube (H8500, Hamamatsu, Japan) as the detector. And also, for proof of our concept, we performed preliminary experiment using pinhole SPECT and brain phantom. The reconstruction ROI contained the region outside the brain, that is, zero count as the priori knowledge. The truncated data were reconstructed by TC-3DOSEM. The reconstructed image without artifact and overestimation was obtained with high resolution. This preliminary experiment suggested feasibility of high resolution and quantitative SPECT for imaging a selected small ROI of human brain.**

Manuscript received November 13, 2009. This work was supported in part by the Grant-in-Aid for Scientific Research (C) (20500435) of the Ministry of Education, Culture, Sports and Technology (MEXT), Japan, the Grant for Translational Research from the Ministry of Health, Labour and Welfare (MHLW), Japan, Newly Adopted Projects of Regional R&D Programs for FY2008 from Kansai Bureau of Economy, Trade and Industry, Japan.

T. Zeniya, Y. Hirano, K. Ishida, H. Watabe, N. Teramoto and H. Iida are with the Department of Investigative Radiology, Advanced Medical Engineering Center, National Cardiovascular Center Research Institute, 5-7-1 Fujishirodai, Suita, Osaka 565-8565 Japan (e-mail: zeniya @ri.ncvc.go.jp).

T. Sakimoto and K. Minato with the Graduate School of Information Science, Nara Institute of Science and Technology, Japan.

H. Kudo is with the Department of Computer Science, Graduate School of Systems and Information Engineering, University of Tsukuba, Japan.

J. Hatazawa is with the Department of Nuclear Medicine and Tracer Kinetics, Osaka University Graduate School of Medicine, Japan.

I. Introduction

We designed a concept of high resolution and quantitative SPECT for imaging a selected small region-of-interest (ROI) of human brain. This system is aimed at achieving high resolution less than 1 mm and being applied for imaging neurons and evaluating drug delivery system. Also, for proof of our concept, we carried out preliminary experiment using pinhole SPECT and brain phantom.

II. Conceptual Design

Pinhole or cone-beam collimators are useful for high-resolution imaging of small ROI. However, as shown in Fig. 1, when the reconstruction ROI is smaller than the object like human brain, the projection data are truncated by radioisotope outside ROI. Because of this truncation, the voxel value of the reconstructed image is overestimated. This hampers quantitative assessment of physiological functions.

Recently, Kudo et al proposed reconstruction theory to solve the interior problem in computed tomography (CT) [1]. We are applying it for pinhole and cone-beam SPECT. Let's explain how to realize with Fig. 2. According to Kudo's theory, the truncated data can be successfully reconstructed within ROI by fulfilling the condition that ROI contains a priori knowledge. In addition to small field-of-view (FOV) detector for imaging with high resolution, we are introducing the parallel-hole collimator attached large FOV detector covering the entire brain to acquire the non-truncated data, even if the resolution of the detector is low. As another condition, the reconstruction matrix must be larger than the object.

Figure 3 is a conceptual illustration of high resolution and quantitative SPECT system for imaging a selected small ROI of human brain. This system has two types of detectors. One is pinhole or cone-beam collimator attached $LaBr_3$(Ce) scintillator with high intrinsic spatial resolution of approximately 1 mm [2] for imaging a selected small ROI with high resolution. The other is parallel-hole collimator attached NaI(Tl) scintillator with active area of 250 mm×150 mm for acquiring the non-truncated data. Position-sensitive photomultiplier tubes (H8500, Hamamatsu, Japan) are optically coupled to both scintilators.

9781-4244-3962-1/09/$25.00 ©2009 IEEE

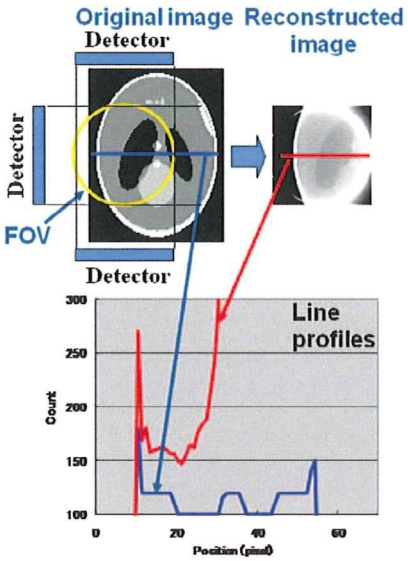

Fig. 1. The artifact and overestimation on the reconstructed image due to truncation.

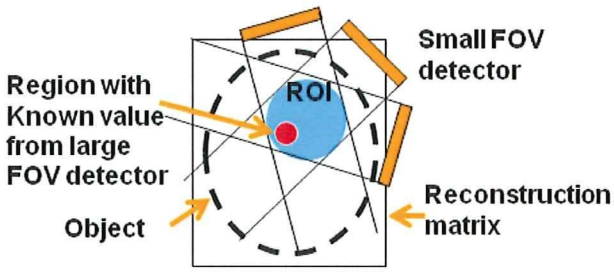

Fig. 2. Schematic diagram showing the solution of the interior problem.

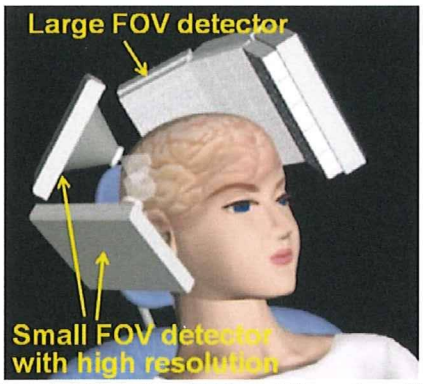

Fig. 3. Conceptual illustration of high resolution and quantitative SPECT system for imaging a selected small ROI of human brain.

III. Preliminary Experiment

For proof of our concept, we performed preliminary experiment using pinhole SPECT and Hoffman brain phantom [3]. The reconstruction ROI contained the region outside the brain, that is, almost zero count as the priori knowledge [4]. The truncated data were reconstructed by truncation compensated 3D-OSEM (TC-3DOSEM) reconstruction method for pinhole SPECT [5].

Figure 4 shows the experimental setup. We scanned a part of Hoffman brain phantom using the rotating stage and 1-mm pinhole collimator fitted to clinical SPECT gamma camera (GCA7200A, Toshiba, Japan). As for the scan parameters, the phantom was filled with Tc-99m of 1,480 MBq and scanned for 2 hours, the radius of rotation was 95mm, the imaging FOV was 95 mm, and the rotation angle was 180 degrees. This radius of rotation is that collimator doesn't hit again the phantom in case of circular orbit and 180 degrees rotation. And also, we scanned same phantom using parallel collimator to compare in terms of spatial resolution.

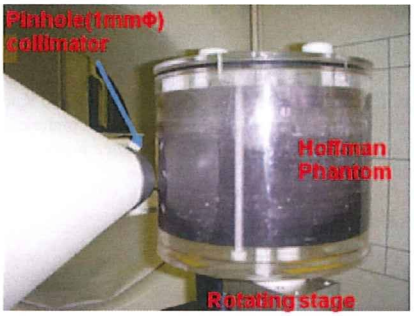

Fig. 4. Experimental setup for scanning Hoffman brain phantom by pinhole SPECT.

Figure 5 shows results of human brain phantom study. In case of clinical SPECT with parallel collimator, the resolution of the reconstructed image was low. In case of pinhole collimator and conventional 3DOSEM, the resolution was high, but the artifact appeared at the edge of ROI and the voxel counts were overestimated. On the other hand, combination of pinhole collimator and TC-3DOSEM provide high resolution image and eliminated the artifact and the overestimation. In this experimental geometry using pinhole collimator, theoretical resolution was approximately 2 mm.

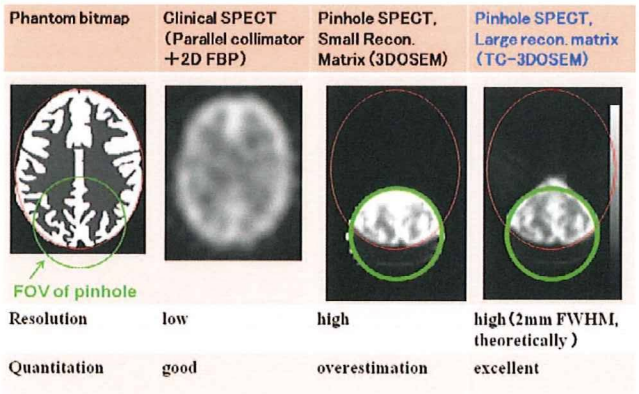

Fig. 5. Comparison of the reconstructed image from preliminary experiment using brain phantom.

IV. Conclusion

We have designed the concept of high resolution and quantitative SPECT for imaging a selected small ROI of human brain. And also, the preliminary experiment suggested

feasibility of high resolution and quantitative SPECT for human brain.

REFERENCES

[1] H. Kudo, M. Courdurier, F. Noo, and M. Defrise, "Tiny a prior knowledge solves the interior problem in computed tomography," *Phys. Med. Biol.*, vol. 53, no. 9, pp. 2207-2231, 2008.

[2] R. Pani, R. Pellegrini, M. N. Cinti, P. Bennati, M. Betti *et al.*, "$LaBr_3$:Ce crystal: The latest advance for scintillation cameras," *Nucl Instrum Meth A.*, vol. 572, pp. 268-269, 2007.

[3] E. J. Hoffman, P. D. Cutler, W. M. Digby, and J. C. Mazziotta, "3D phantom to simulate cerebral blood flow and metabolic images for PET," *IEEE Trans. Nucl. Sci.*, vol. 37, pp. 616-620, 1990.

[4] M. Defrise, F. Noo, R. Clackdoyle, and H. Kudo, "Truncated Hilbert transform and image reconstruction from limited tomographic data," *Inverse Problems*, vol. 22, pp. 1037-1053, 2006.

[5] T. Zeniya, H. Watabe, A. Sohlberg, T. Inomata, H. Kudo, et al., "3D-OSEM reconstruction from truncated data in pinhole SPECT," *2007 IEEE Nuclear Science Symposium Conference Record*, vol. 6, pp. 4205-4207, 2007.

Interior SPECT Reconstruction Problem with Tiny *a proiri* Knowledge – An Application for High Resolution Pinhole Brain Imaging

Qiu Huang, Tsutomu Zeniya, Hiroyuki Kudo, Hidehiro Iida, and Grant T. Gullberg

Abstract— **The quantitation of cerebral blood flow (CBF) and cerebral vascular reactivity (CVR) are valuable in diagnosing brain ischemia, and the quantitation of benzodiazepine receptor density is important in evaluating neuronal damage due to ischemic effects. To better evaluate cerebral autoregulation, a high resolution brain single photon emission computed tomography (SPECT) imager is being built that provides an image of the entire brain for support information in the reconstruction of the interior problem from small field-of-view, truncated projections for high resolution ROI imaging.**

Kudo *et al.* presented a unique and stable solution to the interior problem in computed tomography (CT) given tiny *a proiri* knowledge of the object. In this work we advance their result to the interior reconstruction problem in SPECT where a uniform attenuation map is assumed in brain imaging.

In the theory, differentiation followed by backprojection (DBP) of truncated SPECT data is shown to obtain the truncated weighted Hilbert transform. Then with *a proiri* information on a small part of the region-of-interest (ROI), the other part of the ROI is shown to be available using the projection onto convex sets (PCOS) method. Simulations show that the algorithm provides quantitative results for the reconstruction of the fan-beam tomographic data. Iterative reconstruction of the pinhole data is under investigation to verify the accuracy of the central slice and to provide reasonable results for regions off the central slice.

Index Terms—**interior problem, SPECT, uniform attenuation, brain imaging.**

I. Introduction

The Department of Investigative Radiology at the National Cardiovascular Center Research Institute in Osaka, Japan is designing a high resolution single photon emission computed tomography (SPECT) imager for obtaining high resolution brain scans for various imaging diagnostic applications. The camera consists of one large field of view detector imaging the whole brain and multiple smaller field of view high resolution detectors imaging small regions of the brain (see Fig. 1). The large field of view detector provides images without truncation that localize areas of particular diagnostic interest and provide support information for the reconstruction of high resolution regions of interest (ROIs) from high resolution truncated projections obtained with the small field of view detectors. The work presented in this paper develops an algorithm that accurately reconstructs uniformly attenuated truncated projections, which is an extension of the interior reconstruction problem for the reconstruction of non attenuated truncated projections.

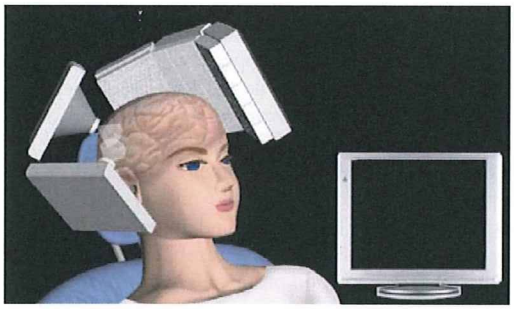

Figure 1. Large field of view detector for imaging whole brain and smaller field of view detectors for imaging ROIs.

The Department of Investigative Radiology has been involved in a large-scale multicenter clinical study aimed at evaluating validity and impact of a quantitative SPECT reconstruction package (QSPECT) [1] for multicenter clinical studies. The quantitative SPECT reconstruction package provides quantitative functional parametric images which are consistent among different setup of equipments and institutions. This allows the use of SPECT in a large scale clinical evaluation for diagnosing brain autoregulatory abnormalities. (A review of noninvasive diagnostic tests to assess cerebral autoregulation can be found in [2].) Dynamic SPECT scans are used to quantify cerebral blood flow (CBF) and cerebral vascular reactivity (CVR) in a single session using a split dose administration of ^{123}I iodo-amphetamine (IMP); one at rest and one during Diamox challenge [3]. Clinical data using QSPECT demonstrated that CBF at rest and during Diamox was reproducible among institutions.

This work was supported in part by the National Institutes of Health under Grant R01 EB00121, and in part by the Director, Office of Science, Office of Biological and Environmental Research, Medical Sciences Division of the U.S. Department of Energy under Contract DE-AC02-05CH11231.

Qiu Huang is with Lawrence Berkeley National Laboratory, One Cyclotron Road, MS 55R0121, Berkeley, CA 94720-8119. (phone: 510-495-2714; fax: 510-486-4768; e-mail: qhuang@lbl.gov).

Tsutomu Zeniya is with the National Cardiovascular Center Research Institute, Suita, Osaka, Japan (e-mail: zeniya @ri.ncvc.go.jp).

Hiroyuki Kudo is with University of Tsukuba, Tsukuba, Japan (e-mail: kudo@*is*.tsukuba.ac.jp).

Hidehiro Iida is with the National Cardiovascular Center Research Institute, Suita, Osaka, Japan (e-mail: iida@ri.ncvc.go.jp).

Grant T. Gullberg is with Lawrence Berkeley National Laboratory, One Cyclotron Road, MS 55R0121, Berkeley, CA 94720-8119. (e-mail: gtgullberg@lbl.gov).

Another important part of the multi-center trial is to evaluate neuronal damage due to ischemia and to provide prognostic value for surgical outcomes. Damage of benzodiazepine receptors has been found in cases of patients with severe brain ischemia [4]. Also, alterations of central benzodiazepine receptors have been described in several neuropsychiatric conditions, including epilepsy, Alzheimer's disease, Huntington's chorea and schizophrenia. Carbon-11-flumazenil, a benzodiazepine antagonist, has been used as a PET radiotracer for visualization and quantification of benzodiazepine receptors in humans. Recently, an iodinated analog of flumazenil, iomazenil has been introduced as a SPECT radiotracer. SPECT imaging of iodine-123-iomazenil (Iomazenil) binding to benzodiazepine receptors in the brain is being used to evaluate neuronal damage caused by ischemia [4] and the prognosis prior to carotid endoarterectomy [5]. Kinetic model-based methods have been developed for SPECT to quantitatively measure ^{123}I-iomazenil binding to benzodiazepine receptors in the human brain [6].

The Department of Investigative Radiology is developing a camera that will perform high resolution imaging of local ROIs in the brain to better address these imaging applications. Imaging with a high resolution small field of view camera provides truncated projections. The reconstruction of these projections involves determining the solution to the interior problem in local tomography. The interior problem in medical imaging refers to the situation where the region-of-interest (ROI) is totally contained within the object. For instance, in SPECT, the interior problem happens when the projections passing through the region outside the ROI are truncated due to a small field-of-view detector or a short detector-to-object distance in the case of converging collimation. The interior problem has been studied for some time [7]. Recently, Kudo *et al.* [8] proved that the solution is unique and stable in computed tomography (CT) if a small region in the ROI is known *a proiri*. In this paper this result is extended to the SPECT interior reconstruction problem.

Both in the work of Kudo *et al.* and in the work presented in this paper, the theory for the solution to the interior problem is based on the differentiation backprojection (DBP) method. The concept of DBP was first developed in parallel beam [9] and cone-beam [10] geometry in CT. The non interior truncation problem was solved for CT in [11], [12], [13], [14], [15]. Similar works in SPECT can be found in [16], [17], [18], [19], [20], where uniform attenuation was assumed. In SPECT the assumption of uniform attenuation is reasonable for some applications such as in brain imaging [21]. The result of the work in this paper shows that, with *a proiri* information of the ROI, the brain image can be reconstructed even when the imaging geometry forms an interior problem. It is expected that this result is useful in the reconstruction of pinhole data, where a pinhole collimator is attached to the small field-of-view cameras for imaging the brain. The pinhole collimator provides a small field-of-view (FOV) with high sensitivity and high resolution when located close to the object.

The paper is organized as follows: Section II shows that the differentiated backprojection (DBP) of fan-beam data is related to the distribution of the radioactive tracer in SPECT through a truncated weighted Hilbert transform. Then a unique inversion is shown to exist for the truncated weighted Hilbert transform given a small region of ROI is known *a proiri*. The results of numerical simulations are presented in Section III where the theory is shown to give a measure of confidence for the quantitative accuracy of the fan-beam reconstruction problem and the conclusion is given in Section IV.

II. Method

The method in this work is illustrated by showing that the differentiated backprojection (DBP) of fan-beam data is related to the distribution of the radioactive tracer in SPECT through a truncated weighted Hilbert transform and the truncated weighted Hilbert transform can be inverted given some prior information.

A. DBP operation for fan-beam data

For a transaxial slice, let $f(x,y)$ represent the distribution of the radiopharmaceutical in body tissues, which is assumed to be a smooth and compactly supported function of R^2. The SPECT image reconstruction estimates $f(x,y)$ from the detected photon counts. We denote $\vec{r}=(x,y)$ and $D=\{(x,y)\in R^2:\ x^2+y^2\le 1\}$. We assume $f(x,y)\equiv 0$ outside of D and the attenuation μ of the body tissues is uniform inside D. A typical fan-beam data acquisition geometry with a circular focal-point trajectory is shown in Fig. 2, where each projection ray is represented by (β,σ). One particular projection ray is shown emanating from the focal point S for the angle β with the ray angle σ.

In this paper, the fan-beam uniformly attenuated projection of the function $f(x,y)$ is defined as

$$[D_\mu f](\beta,\sigma)=\int_0^\infty f(S+\tau\vec{\alpha}(\beta,\sigma))e^{\mu\tau}d\tau\,, \qquad (1)$$

where $D_\mu f$ is the projection operator for the uniformly attenuated fan-beam projection data, $\sigma\in[-\sigma_m,\sigma_m]$, and $\vec{\alpha}(\beta,\sigma)$ is a unit vector in R^2 representing the direction from the focal point to the collimation hole, as shown in Fig. 2. Here, $\sigma_m\in(0,\pi/2)$ denotes the maximum angle subtended by the fan-beam. Let R be the radius of the circular focal point trajectory. We can modify the fan-beam data to obtain:

$$g(\beta,\sigma)=e^{-\mu R\cos\sigma}[D_\mu f](\beta,\sigma)\,. \qquad (2)$$

Define

$$s=R\sin\sigma,\quad \theta=\sigma+\beta$$

$$\hat{\sigma}(r,\varphi,\theta)=\arcsin\frac{\vec{r}\cdot\vec{\theta}}{R}=\arcsin\frac{r\cos(\theta-\varphi)}{R}\,.$$

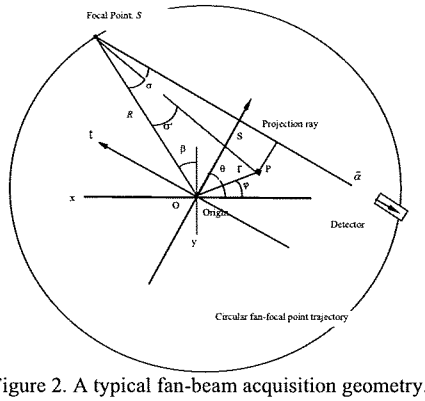

Figure 2. A typical fan-beam acquisition geometry.

We denote $\vec{\theta} = (\cos\theta, \sin\theta)$ and $\vec{\theta}^{\perp} = (-\sin\theta, \cos\theta)$ and construct an image:

$$\hat{f}(x,y) = -\frac{1}{2}\int_{-\pi/2}^{\pi/2} \frac{e^{i\omega\cdot\vec{\theta}^{\perp}}[(\frac{\partial}{\partial\sigma}-\frac{\partial}{\partial\beta})g](\theta-\hat{\sigma}(r,\varphi,\theta),\hat{\sigma}(r,\varphi,\theta))}{R\cos\hat{\sigma}(r,\varphi,\theta)}d\theta. \quad (3)$$

This image was proved to be related to the original distribution of radiopharmaceutical as [17]:

$$\hat{f}(x,y) = \int_{-\infty}^{\infty} \frac{\cosh(\mu\tau)f(x-\tau,y)}{\pi\tau}d\tau. \quad (4)$$

Equation (3) involves the operations of derivative and backprojection for the modified attenuated projection in fan-beam geometry and can be readily obtained from fan-beam measurements. Equation (4) shows that the image $\hat{f}(x,y)$ is an image obtained by convolving the true image with a one-dimensional (1D) kernel $\cosh(\mu t)/(\pi t)$ multiplied by some factor, thus the image reconstruction is accomplished by inverting the convolution corresponding to a truncated weighted Hilbert transform.

B. Inversion of Truncated Hilbert Transform

Denote the left hand side of (4) by $g(t)$ and the distribution of activity by $f(t)$. The reconstruction is to solve the following integral equation:

$$g(t) = \int_{-1}^{1} \frac{\cosh(\mu\tau)f(t-\tau)}{\pi\tau}d\tau.$$

As shown in Fig. 3, the function $f(t)$ has a support in $-1<t<1$. There is no loss of generality since shifting and scaling can always transform any support interval to $(-1,1)$.

If $g(t)$ is known for $-1<t<1$, the equation can be solved as in [19] and [17]. Unfortunately, for some geometries the function $g(t)$ is only available on a small interval $-1<a<t<d<1$. Then the algorithms in [19] and [17] do not guarantee a stable inversion. However, based on the work by Kudo et al [8], we

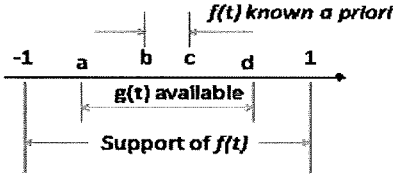

Figure 3. Illustration of intervals.

found if the value of $f(t)$ in the interval $a<b<t<c<d$ is assumed to be known, then the inversion is available in (a,d).

The reconstruction problem becomes:

$$g(t) = \int_{-1}^{1} \frac{\cosh(\mu\tau)f(t-\tau)}{\pi\tau}d\tau \quad . \quad (-1<a<t<d<1), \quad (5)$$

subject to $f(t) = f^{(p)}(t)$ for $(a<b<t<c<d)$.

According to [17], we know the inversion can be obtained by constructing a new function from $g(t)$:

$$\int_{-1}^{1} \frac{g(s)}{\pi(s-t)}\frac{\sqrt{1-t^2}}{\sqrt{1-s^2}}ds.$$

In this case, this function can be broken into two terms: $h_1(t)+h_2(t)$, where

$$h_1(t) = \int_{a}^{d} \frac{g(s)}{\pi(s-t)}\frac{\sqrt{1-t^2}}{\sqrt{1-s^2}}ds,$$

$$h_2(t) = \left(\int_{-1}^{a} . + \int_{d}^{1} .\right)\frac{g(s)}{\pi(s-t)}\frac{\sqrt{1-t^2}}{\sqrt{1-s^2}}ds.$$

The first term $h_1(t)$ is available from the truncated weighted Hilbert transform $g(t)$ for $a<t<d$, while the second term $h_2(t)$ remains unknown.

Since the function $f(t)$ is known for $b<t<c$, the second term in this interval can be represented as

$$h_2(t) = \left[\left((I+\Phi)f^{(p)}\right)\right](t) - h_1(t) \qquad \text{for} \qquad t\in(b,c).$$

Here, the operator Φ is the same as in [17] and I indicates the unity operator.

According to the continuity property of analytical functions, the function $h_2(t)$ can be analytically continued from the known interval (b, c) on the real axis to the larger interval (a, d) on the real axis. Since both $h_1(t)$ and $h_2(t)$ are uniquely determined for $t\in(a,d)$, function $f(t)$ is uniquely determined for $t\in(a,d)$. Then the projection onto convex sets (PCOS) method [22] was used to solve the integral equation in (5). Numerical results will be shown in the next section.

III. NUMERICAL RESULTS

In the fan-beam SPECT simulation study, the object image is chosen to be the modified Shepp-Logan phantom shown in Fig. 4. Uniform attenuation coefficient $\mu=0.15cm^{-1}$ was chosen to generate the truncated attenuated fan-beam data.